J. Fluid Mech. (1997), *vol.* 338, *pp.* 89–126

Experimental assessment of fractal scale similarity in turbulent flows. Part 2. Higher-dimensional intersections and non-fractal inclusions

By RICHARD D. FREDERIKSEN,[1] WERNER J. A. DAHM[1] AND DAVID R. DOWLING[2]

[1] Department of Aerospace Engineering, The University of Michigan, Ann Arbor, MI 48109-2118, USA

[2] Department of Mechanical Engineering and Applied Mechanics, The University of Michigan, Ann Arbor, MI 48109-2125, USA

(Received 6 April 1996 and in revised form 11 September 1996)

Results from an earlier experimental assessment of fractal scale similarity in one-dimensional spatial and temporal intersections in turbulent flows are here extended to two- and three-dimensional spatial intersections. Over 25000 two-dimensional (256^2) intersections and nearly 40 three-dimensional (256^3) intersections, collectively representing more than 2.3 billion data points, were analysed using objective statistical methods to determine which intersections were as fractal as stochastically scale-similar fractal gauge sets having the same record length. Results for the geometry of $Sc \gg 1$ scalar isosurfaces and the scalar dissipation support span the range of lengthscales between the scalar and viscous diffusion scales λ_D and λ_ν. The present study finds clear evidence for stochastic fractal scale similarity in the dissipation support. With increasing intersection dimension n, the data show a decrease in the fraction of intersections satisfying the criteria for fractal scale similarity, consistent with the presence of localized non-fractal inclusions. Local scale similarity analyses on three-dimensional (64^3) intersections directly show such intermittent non-fractal inclusions with characteristic lengthscale comparable to λ_ν. These inclusions lead to failure of the relation among codimensions $D_n \equiv D-(3-n)$ when applied to simple average dimensions, which has formed the basis for most previous assessments of fractal scale-similarity. Unlike the dissipation support geometry, scalar isosurface geometries from the same data were found not to be as fractal as fractional Brownian motion gauge sets over the range of scales examined.

1. Introduction

One of the central objectives of turbulence theory involves identifying the proper similarity rules that characterize scalar and velocity fluctuations over lengthscales and timescales sufficiently removed from external influences for the natural scale-equilibrium to be established. The first partially successful attempt at this was Kolmogorov's (1941) similarity hypothesis, which still forms the cornerstone of turbulence theory. Kolmogorov's (1962) modification based on intermittency corrections to his original ideas provided the next major advance in understanding turbulence-similarity scaling. Roughly twenty years later, concepts from nonlinear dynamics provided a potential framework for refined similarity hypotheses of turbulent flows. These have led to modern developments in the subject that focus

largely on fractal and multifractal scaling models of various aspects of turbulence fields. However, direct evidence for the applicability of this broad class of scale similarity hypotheses to turbulent flows has been limited, and has led to mixed conclusions regarding the validity of modelling the equilibrium scale similarity using these concepts. The present study is intended to provide an objective assessment of the applicability, over at least a limited range of scales, of fractal scale similarity in turbulent flows.

Previous studies (Sreenivasan & Prasad 1989; Prasad & Sreenivasan 1990*a*; Sreenivasan 1991; Lane-Serff 1993) have investigated fractal properties of higher-dimensional intersections with the scalar isosurface field. These have found fractal scale similarity to be present in two-dimensional spatial intersections with scalar isosurface fields produced by turbulent flows, however, considerable variation in the dimension was seen with different isosurface threshold values. Further work by Prasad & Sreenivasan (1990*b*) extended their analysis to three spatial dimensions and produced results consistent with their previous two-dimensional analyses. Investigations of the possible fractal scale similarity of two- and three-dimensional intersections with the scalar energy dissipation support are limited to the work of Prasad, Meneveau & Sreenivasan (1988), Sreenivasan & Prasad (1989), Sreenivasan (1991), and Prasad & Sreenivasan (1990*b*). The results of these studies all found the scalar dissipation field to exhibit multifractal characteristics and thus would be consistent with a fractal scalar dissipation support.

Much of this existing experimental evidence was summarized in an earlier companion paper (Frederiksen, Dahm & Dowling 1996), hereinafter referred to as Part 1. That paper presented independent experimental assessments for the applicability of uniform fractal scale similarity to certain geometric properties of one-dimensional intersections with $Sc \gg 1$ conserved scalar fields $\zeta(\boldsymbol{x}, t)$ in turbulent flows. That study introduced objective statistical methods for determining whether or not a given data record with finite length was 'as fractal as a known fractal gauge set having the same record length'. Criteria were established for comparisons with deterministically self-similar fractal gauge sets, represented by the class of irregular Cantor sets, as well as with stochastically self-similar fractals characterized by the fractional Brownian motion (fBm) set. Analyses were conducted on one-dimensional spatial and temporal intersections through fully-resolved three- and four-dimensional data spanning from the scalar diffusion scales (λ_D, T_D) across the viscous diffusion scales (λ_ν, T_ν) to the outer scales (δ, T_δ).

The results in Part 1 from over two million such one-dimensional intersections with isosurfaces in the conserved scalar field $\zeta(\boldsymbol{x}, t)$ at scales between (λ_D, T_D) and (λ_ν, T_ν) did not show the required approach to constant dimension indicative of strict scale-similarity, either deterministic or stochastic. Over this inner range of scales, the scalar isosurface geometries displayed a scaling that at best approximated the similarity in fBm sets with dimension $D_1 = 0.48 \pm 0.12$ for all isoscalar values. However, at scales between the viscous and outer scales, no uniform scale similarity consistent with either deterministically or stochastically self-similar fractals was found in scalar field isosurfaces.

In contrast, the spatio-temporal support geometry on which the scalar dissipation field $\boldsymbol{\nabla}\zeta \cdot \boldsymbol{\nabla}\zeta(\boldsymbol{x}, t)$ is concentrated was found to display uniform scale similarity comparable with stochastically self-similar fBm sets having dimension $D_1 = 0.66 \pm 0.05$ over the entire range from the inner scales (λ_D, T_D) to the outer scales (δ, T_δ). This support dimension was found to decrease with increasing dissipation threshold values, as a direct consequence of the decreasingly space-filling nature of the dissipation field

with increasing threshold. This latter issue is itself closely connected with possible multifractal scaling in the dissipation field, and is examined in a Part 3 companion paper (Frederiksen, Dahm & Dowling 1997). The difference in applicability of fractal scale similarity to the geometry of scalar isosurfaces and the dissipation support was attributed to the differing retention of information in the scalar and dissipation fields that results from their respective underlying dynamics.

Part 1 pointed to several possible reasons for the different finding in that study and results from other studies concerning the applicability of fractal scale similarity to scalar isosurfaces. These included the anticipated break in similarity across the viscous diffusion scales (λ_ν, T_ν), as well as the potential influence of inner and outer cut-offs in the range of scales examined. However, these were discounted by the fact that the scalar dissipation support from precisely the same data showed clear applicability of fractal scaling over precisely the same range of scales. It was concluded that the findings differed from preious results as a result of the objective statistical criteria used to determine if an ensemble of intersections displayed scale similarity consistent with fractal gauge sets having the same record length.

The present study extends the results from Part 1 to higher-dimensional intersections to clarify the geometric scaling properties of isoscalar surfaces and the dissipation support in $Sc \gg 1$ conserved scalar fields in turbulent flows. Such higher-dimensional intersections permit more precise assessments of scale similarity owing to the comparatively greater information contained in the two-dimensional (256^2) and three-dimensional (256^3) experimental data sets used here than in the 256-point and 4096-point one-dimensional intersections examined in Part 1. More importantly, the present higher-dimensional assessments allow access to the local scale similarity parameter $Q(\boldsymbol{x}, t)$ and the local fractal dimension $D(\boldsymbol{x}, t)$ throughout each data volume. As will become evident below, these directly show the presence of non-fractal inclusions in an otherwise fractal background structure. Equally important and closely connected with this, such higher-dimensional analyses do not rely on the method of intersections (e.g. Feder 1988) relating codimensions D_n in lower n-dimensional intersections through uniform fractal sets to the true fractal dimension D as

$$D \equiv D_n + (3-n),$$

which has formed the basis for most previous assessments of fractal dimension. In fact it will be seen below that significant departures from this relation arise as a consequence of the non-fractal inclusions mentioned above.

Section 2 below summarizes the experimental data used in the present study. Section 3 briefly reviews the statistical criteria developed in Part 1 and discusses their extension to higher dimensions in the present study. Following this, §4 gives calibration results for two-dimensional spatial intersections through stochastically self-similar fBm sets and, based on these, presents assessments of scale similarity in two-dimensional intersections through conserved scalar isosurfaces and scalar dissipation support sets. Analogous calibrations and results for three-dimensional spatial intersections are given in §5. Section 6 examines local scale similarity throughout these three-dimensional spatial data volumes, and presents results showing non-fractal inclusions in these data and characterizes their size and their effect on the applicability of fractal scale similarity. A collective discussion of these results together with those from Part 1 is given in §7, and conclusions are drawn as to the applicability of fractal scale similarity in turbulent flows.

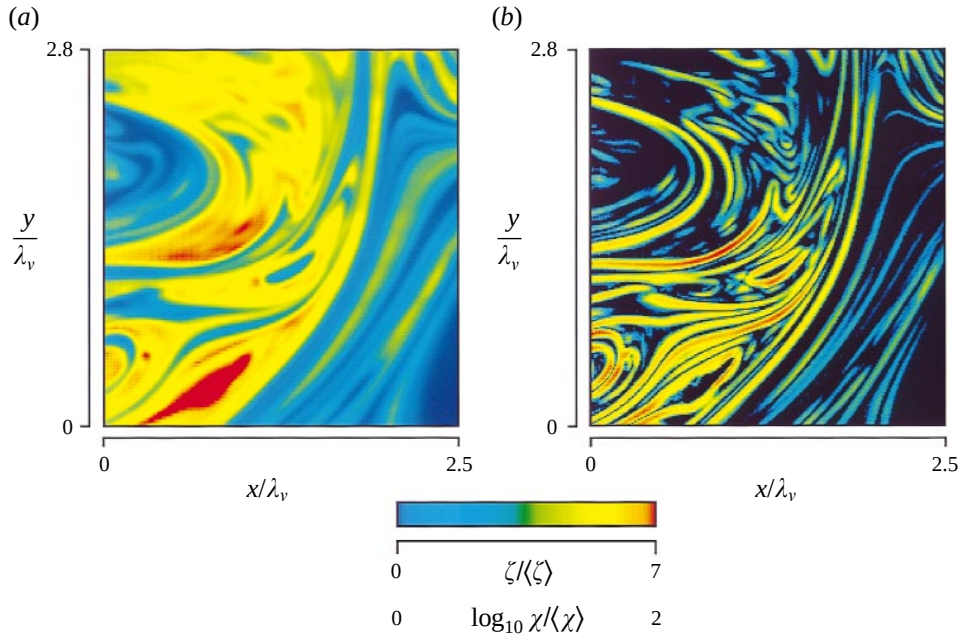

FIGURE 1. An example of a two-dimensional (256^2) spatial data plane, showing (*a*) the scalar field $\zeta(\boldsymbol{x}, t)$ in a typical data plane, and (*b*) the scalar energy dissipation rate field $\chi(\boldsymbol{x}, t) \equiv D\boldsymbol{\nabla}\zeta\cdot\boldsymbol{\nabla}\zeta(\boldsymbol{x}, t)$ in the same plane.

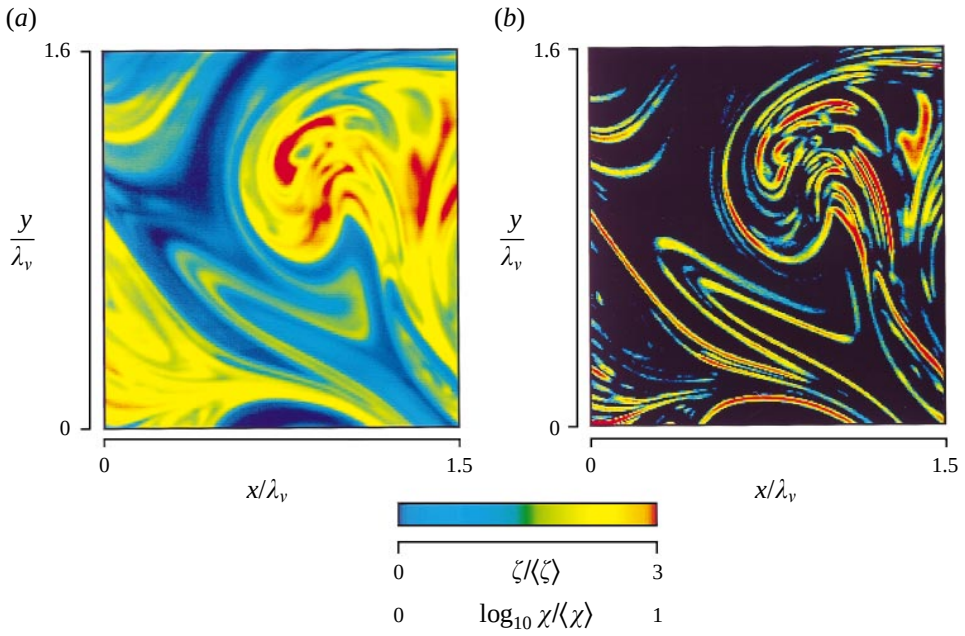

FIGURE 2. Another example of a typical two-dimensional (256^2) spatial data plane, showing (*a*) the scalar field $\zeta(\boldsymbol{x}, t)$ in a typical data plane, and (*b*) the scalar energy dissipation rate field $\chi(\boldsymbol{x}, t) \equiv D\boldsymbol{\nabla}\zeta\cdot\boldsymbol{\nabla}\zeta(\boldsymbol{x}, t)$ in the same plane.

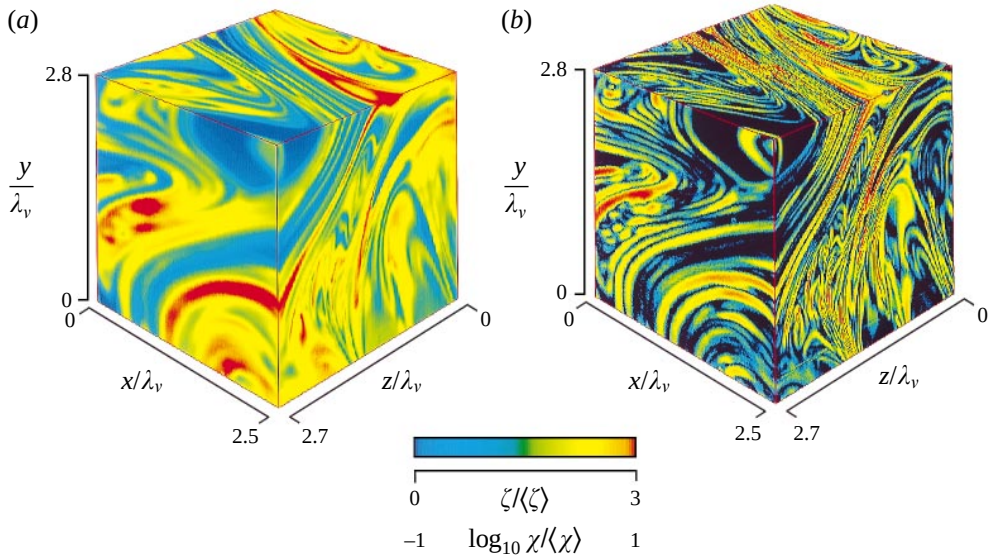

FIGURE 3. An example of a fully resolved three-dimensional (256^3) spatial data volume, showing (*a*) the scalar field $\zeta(\boldsymbol{x}, t)$ in a typical volume, and (*b*) the scalar energy dissipation rate field $\chi(\boldsymbol{x}, t) \equiv D\boldsymbol{\nabla}\zeta \cdot \boldsymbol{\nabla}\zeta(\boldsymbol{x}, t)$ in the same data volume.

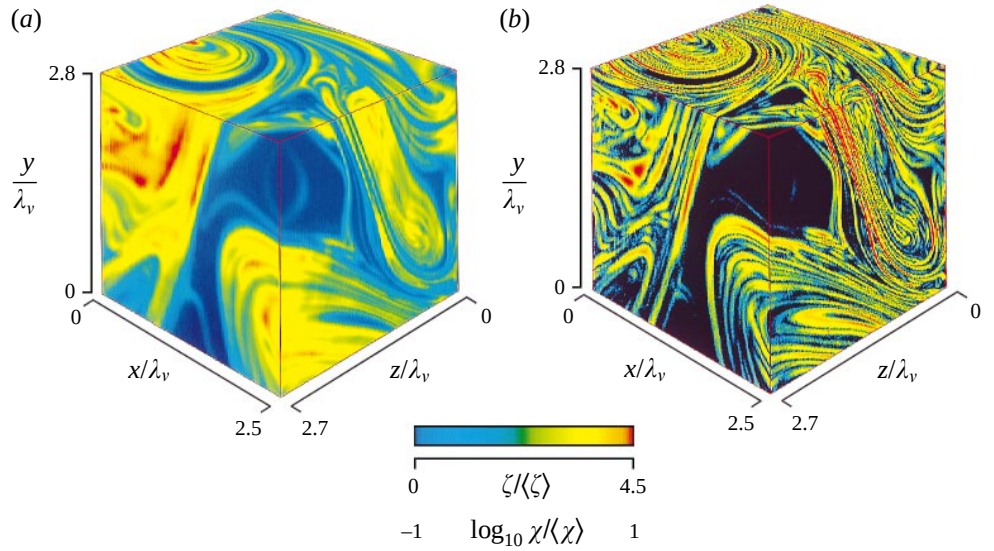

FIGURE 4. Another example of a typical fully resolved three-dimensional (256^3) spatial data volume, showing (*a*) the scalar field $\zeta(\boldsymbol{x}, t)$ in a typical volume, and (*b*) the scalar energy dissipation rate field $\chi(\boldsymbol{x}, t) \equiv D\boldsymbol{\nabla}\zeta \cdot \boldsymbol{\nabla}\zeta(\boldsymbol{x}, t)$ in the same data volume.

2. Data summary

The present study was based on the same three-dimensional (256^3) spatial data volumes as were used in analysing one-dimensional spatial intersections in Part 1. The measurement technique developed to obtain these data is described in detail by Dahm,

			Spatial resolution				Temporal resolution			
Data set	Re_δ	Re_λ	λ_D (μm)	λ_ν (μm)	$\Delta x, \Delta y$ (μm)	Δz (μm)	λ_D/u (ms)	λ_ν/u (ms)	Δt (ms)	ΔT (ms)
R0806	5000	52	209	9520	107	100	62	2820	8.87	2270
R0703	3700	45	257	11700	109	120	103	4690	8.87	2270
R0304	2900	40	309	14100	110	88	158	7200	8.87	2270

TABLE 1. Spatial and temporal resolution characteristics.

Southerland & Buch (1991) and Southerland & Dahm (1994, 1996), and a summary of the resulting data characteristics was given in §2 of Part 1. Briefly, the data are from laser induced fluorescence measurements of $Sc \gg 1$ conserved scalar mixing in the self-similar far field of an axisymmetric turbulent jet in water. The concentration field $\zeta(\boldsymbol{x}, t)$ of a laser fluorescent dye carried by the jet fluid was measured repeatedly in time at up to 256^3 points within a small three-dimensional spatial volume located 235 diameters (1.15 m) downstream of the jet exit and 26 diameters (13 cm) off the jet centreline. A highly collimated laser beam was swept in a raster fashion through this volume, and the resulting laser induced fluorescence from dye-containing fluid was imaged onto a high-speed, planar, 256×256 element, photodiode array. The array output was serially acquired at 8-bits true digital depth and continuously written in real time to a 3.1 GB high-speed parallel-transfer disk bank capable of accommodating more than 50000 such 256^2 data planes. The resulting measured fluorescence intensity field was converted to the true dye concentration as described in Southerland & Dahm (1994, 1996).

Examples of the scalar field in such individual (256^2) spatial data planes are shown in figures 1 and 2. A succession of 256 such 256^2 spatial data planes comprises each of the present three-dimensional (256^3) spatial data volumes of the type shown in figures 3 and 4. Each four-dimensional data set consists of a temporal sequence of up to 200 such individual (256^3) spatial data volumes, giving the scalar field values $\zeta(\boldsymbol{x}, t)$ at over 3 billion points in space and time. The resulting spatial and temporal resolution can be determined by noting that the local outer scale $\delta(x) \approx 0.44x$ and centreline velocity $u(x) \approx 7.2(J/\rho)^{1/2} x^{-1}$, with J the jet source momentum flux and ρ the ambient fluid density. For example, as given in table 1, at a typical outer scale Reynolds number $Re_\delta \equiv (u\delta/\nu) \approx 3700$ and with the Schmidt number of 2075, the local strain-limited molecular diffusion lengthscale estimate is $\lambda_D \approx 257$ μm and its local advection timescale estimate is $T_D \equiv \lambda_D/u \approx 103$ ms. For comparison, the in-plane spatial resolution was $\Delta(x, y) \approx 109$ μm. The $(1/e)$ laser beam thickness was measured as 181 μm. Deconvolution of the scalar field measurements among adjacent planes increases the effective spatial resolution in the z-direction to the interplane separation $\Delta z \approx 120$ μm. These values show that both the characteristic scale of the pixel image volume $(\Delta x\, \Delta y\, \Delta z)^{1/3}$ and its maximum dimension are less than $0.5\lambda_D$. Similarly, the temporal separation between successive data planes was $\Delta t = 8.9$ ms. Comparing with the diffusion scale advection time of 103 ms verifies that the present measurements resolve essentially all of the fine scale structure of the local turbulent mixing process.

In Kolmogorov variables, the local strain-limited molecular diffusion lengthscale $\lambda_D = \lambda_\nu Sc^{-1/2}$, where λ_ν is the local strain-limited viscous diffusion scale, and $\lambda_\nu \approx 5.9\lambda_K$ (Southerland & Dahm 1994, 1996) with the Kolmogorov scale $\lambda_K \equiv (\nu^3/\epsilon)^{1/4}$. Thus the

scalar diffusion lengthscale $\lambda_D = 0.13\lambda_K$, and the scalar diffusion timescale $\lambda_D/u = 0.009\tau_K$, where $\tau_K \equiv (\nu/\epsilon)^{1/2}$ is the Kolmogorov timescale. Even in the worst case, the interplane time of 0.009 s is less than $0.091\lambda_D/u$ and thus is entirely negligible relative to τ_K. Consequently, the data acquisition rate is sufficient to effectively freeze the scalar field, and to entirely freeze the underlying velocity field. The resulting spatio-temporal resolution allows accurate differentiation of the measured conserved scalar field in the three spatial dimensions to determine all three components of the true local instantaneous scalar gradient vector field $\nabla\zeta(\boldsymbol{x}, t)$ throughout these three-dimensional data. This in turn permits determination of the true scalar energy dissipation rate field $\nabla\zeta \cdot \nabla\zeta(\boldsymbol{x}, t)$, as shown in figures 1–4, and thus assessment of the geometric scaling properties of the compact support on which this field is concentrated in turbulent shear flows.

As noted in Part 1, the imaged region in the turbulent scalar field typically spans less than $\frac{1}{15}$ of the local outer scale δ, and is comparable to the local viscous diffusion scale λ_ν of the flow. The structure of velocity and scalar fields in turbulent shear flows at scales near and below λ_ν appears to be statistically universal even for the present moderate Reynolds numbers, as evidenced by Jiménez *et al.* (1993). The estimated Taylor scale Reynolds numbers for the present data are $Re_\lambda \approx 45$, well within the range of values over which the DNS results of Jiménez *et al.* showed Reynolds-number-independent collapse on inner variables of the fine-scale vortical structures of the flow. Moreover, high-wavenumber spatial scalar spectra from these same data (Southerland, Dahm & Dowling 1995) show the k^{-1} scaling predicted by Batchelor for large Sc mixing in turbulent flows. As a result, although the present measurements are from $2900 \leqslant Re_\delta \leqslant 5000$ turbulent jets, the geometric scaling properties of the fine scales contained in them are believed to be largely representative of the scaling properties at the inner scales of all turbulent shear flows.

3. Fractal assessment criteria

This study adopts the statistical box counting algorithm developed in Part 1, but extends this to two- and three-dimensional records. It also uses the same χ^2 statistical goodness-of-fit parameter Q in (4) of Part 1 (see Bevington & Robinson 1992; Press *et al.* 1992) to discern if any given two- or three-dimensional record is 'as fractal as any given fractal gauge set having the same record size' on the basis of threshold Q values determined by applying the box counting algorithm to a set of calibration cases. Higher-dimensional fractional Brownian motion sets are used here as gauge sets, based on the results found from one-dimensional intersections in Part 1. Comparisons with random percolation sets, which in Part 1 served as negative gauge sets displaying no scale similarity, play a much smaller role in the present study. Such random constructions in their present higher-dimensional forms were found to produce sets that were manifestly different from any of the experimental records examined. Results in Part 1 also verified that these fractal assessment criteria were effectively insensitive to noise even at levels many times higher than in the present data.

A given record is determined either to be or not to be as fractal as an fBm set having the same average dimension and record size on the basis of its local fractal dimension $D(\epsilon)$ given in (2) of Part 1, and from its $\langle D(\epsilon)\rangle$ and Q coordinates, in precisely the same manner as described in Part 1. (The fractal assessment criterion must depend on D since the scaling quality varies with dimension, as has also been noted by Sreenivasan & Juneja 1993.) In the two-dimensional results that follow in §4 and the three-

dimensional results in §5, calibrations for each of these criteria are first presented for stochastically self-similar fBm sets, and then corresponding results from analyses of experimental data records are compared against these.

It should be noted, however, that extension of these fractal scale-similarity criteria from Part 1 becomes computationally time consuming as the intersection dimension n is increased. Construction of higher-dimensional fBm gauge sets with record size N in each of n dimensions involves combining n one-dimensional fBm sets of record length N, yielding an N^n increase in the number of summation and level-crossing construction steps. Similarly, in applying the box-counting technique itself to these gauge sets (and to the data as well), the number of points that must be interrogated at each scale of the analysis increases as N^n. This increase in the time needed for creation and analysis of each realization of every gauge set required reducing the total number of sets used for calibration from over 100000 for the one-dimensional 256-point assessments in Part 1 to just 200 for the three-dimensional 256^3 assessments in the present study. Even with this reduction, the total time required for each of the present three-dimensional calibrations is more than 130 times that for each of the one-dimensional calibrations in Part 1.

The same scaling with intersection dimension also necessitated reducing the number of data records that could be analysed from several million (256-point) intersections for the one-dimensional assessments to just 25000 (256^2-point) intersections in the present two-dimensional assessments, and to just 40 (256^3-point) intersections in the present three-dimensional assessments. The smaller number of independent intersections would increase statistical uncertainty levels, but this was more than offset by the attendant increase in certainty with which any given higher-dimensional set could be judged to be fractal or non-fractal. The results below are from scale-similarity assessments that collectively represent over 2.3 billion points from the three cases listed in table 1, with the data from each case typically spanning 10–25 inner timescales λ_ν/u while still permitting time variations on the order of the inner scale to be seen in volume-to-volume comparisons.

4. Two-dimensional intersections

This section presents results from two-dimensional intersections through isosurface sets from conserved scalar fields $\zeta(\boldsymbol{x}, t)$ of the type in figures 1(*a*) and 2(*a*), and through support sets for scalar energy dissipation rate field $\boldsymbol{\nabla}\zeta\cdot\boldsymbol{\nabla}\zeta(\boldsymbol{x}, t)$ of the type in figures 1(*b*) and 2(*b*), for each of the cases listed in table 1. Criteria based on the scale similarity displayed by stochastically self-similar two-dimensional fBm sets, constructed from superpositions of lower-dimensional fBm sets, are developed in §4.1. Results for the geometric scaling properties of the dissipation support are given in §4.2, and for the scaling properties of scalar isosurfaces in §4.3.

4.1. *Two-dimensional calibrations*

Two-dimensional calibrations were performed with fBm gauge sets having dimensions $1 < D < 2$ in increments of $\Delta D = 0.1$. As an example, the $D(\epsilon)$ signatures of 1000 individual realizations of two-dimensional (256^2) fBm sets, each having $D \equiv 1.5$, are presented in figure 5(*a*). As was seen in Part 1, as the box size $(\epsilon/L) \to 0$ the $D(\epsilon)$ results asymptote toward constant values around the true dimension. Notice that the $D(\epsilon)$ results in figure 5(*a*) show much faster convergence to the true dimension than did the corresponding one-dimensional fBm sets in figure 5(*b*) of Part 1. This is to be expected,

since the scaling information contained in each two-dimensional (256^2) record is much greater than in the corresponding one-dimensional (256-point) records of Part 1.

For any two-dimensional record composed of $p \times p$ equally spaced points, the smallest accessible box size is $(\epsilon/L) = 1/p$. Thus for the present 256^2 two-dimensional spatial data planes, the $D(\epsilon)$ results are confined to $2 \leqslant -\log_2(\epsilon/L) \leqslant 7$. As in Part 1, this accessible range of scales is separated into two regions (termed Regions 1 and 2), the former dominated by the decrease in $D(\epsilon)$ at relatively large box sizes, and the latter in which an asymptotic approach to constant $D(\epsilon)$ becomes evident. The standard deviation σ in $D(\epsilon)$ over Region 2 and the average value $\langle D(\epsilon)\rangle$ over the same range of scales provide a means for assessing if a given set displays scale similarity comparable to an fBm set having the same average dimension over the same range of scales. Results obtained from such calibrations for fBm sets covering the range of true dimensions from $1 < D < 2$ are given in table 2. Note that, in contrast to the one-dimensional gauge sets considered in Part 1, here σ does not vary strongly with $\langle D(\epsilon)\rangle$.

Each individual realization in figure 5(*a*) produces a single Q value and an average $D(\epsilon)$ value over Region 2. Collecting joint $\langle D\rangle$ and Q statistics over all realizations and all dimensions produces the cumulative distributions in figure 5(*b*). As in Part 1, the contours denote cumulative probability boundaries, with 50% of the fBm sets producing $\langle D\rangle$ and Q values to the right-hand side of the solid 0.5 contour, 95% producing values to the right-hand side of the solid 0.05 contour, etc. Also shown are the corresponding contours for random percolation sets having the same relative cover, where 99% of the random sets produced $\langle D\rangle$ and Q values to the left-hand side of the dashed 0.99 contour, etc. Note that in these two-dimensional calibrations the random and fractal contours cross much closer to the limiting D value (here 2) than was the case in the one-dimensional calibrations in figure 5(*b*) of Part 1. In effect, it is much less likely that random percolation will produce a set that displays fractal scale similarity in two dimensions than was the case in one dimension. Except at these extremely large values, there is a clear separation between the Q values obtained from fractal and random sets, allowing an objective statistical determination of the probability that a given two-dimensional (256^2) data record displays scale similarity 'as fractal as an fBm set having the same record length and dimension', or 'as random as a percolation set having the same record length and dimension'.

4.2. *Scalar dissipation support intersections*

The scalar dissipation support consists here of all points where the scalar dissipation field $\nabla\zeta\cdot\nabla\zeta(\boldsymbol{x}, t)$ is above the mean dissipation value. Effects of varying this dissipation threshold value were examined in Part 1. Figures 6 and 7 each present results from analyses of the scale similarity properties of the dissipation support for cases R0703 and R0304 in table 3. Each of these figures represents ensemble statistics collected from nearly 10000 individual two-dimensional intersections of the type in figures 1(*b*) and 2(*b*). These intersections are taken through thirteen different 256^3 spatial data volumes of the type in figures 3(*b*) and 4(*b*), spanning the range of scales between the scalar diffusion scale λ_D and the viscous diffusion scale λ_ν. The typically thirteen spatial data volumes analysed in each case were spaced in time by about one to two viscous diffusion timescales λ_ν/u, depending on the case analysed (see table 3). This temporal separation ensures marginal statistical dependence between successive volumes analysed, allowing time variations to be identified on a volume-to-volume basis but still yielding a statistically meaningful sample among the volumes analysed. Moreover, it will be seen below that the scale-similarity properties of these data show significant variations among the three cases considered.

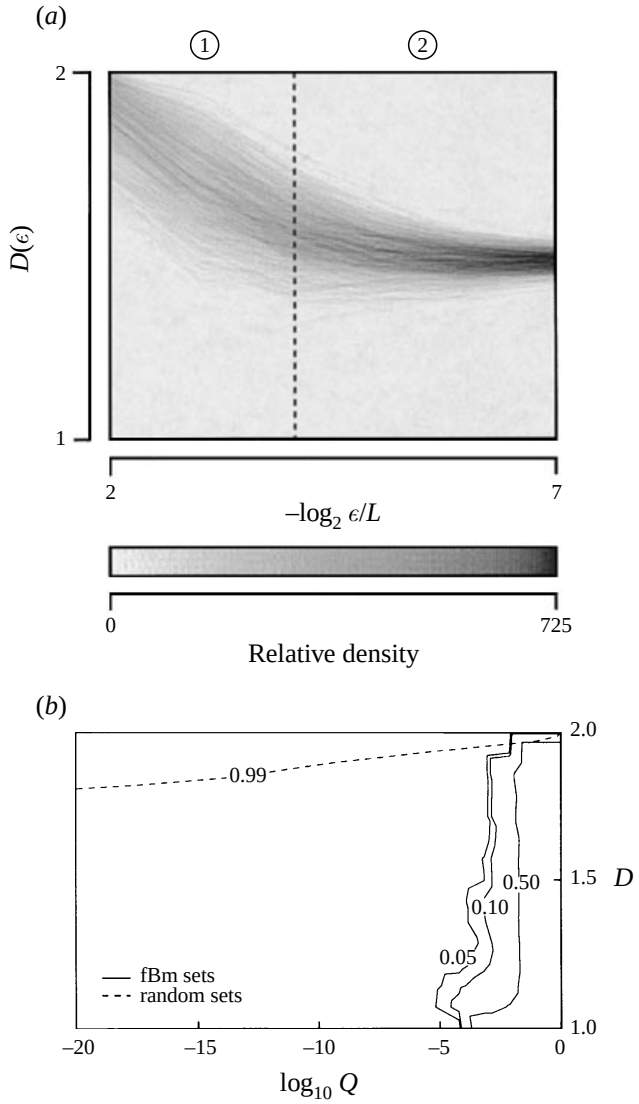

FIGURE 5. $D(\epsilon)$ results from (a) fractional Brownian motion sets with $D = 1.5$ and (b) the corresponding fractal criterion developed from analysis of many two-dimensional fractional Brownian motion sets.

Figures 6(a) and 7(a) give the ensemble results for the dimension $D_2(\epsilon)$ obtained from these two-dimensional intersections for these two cases, and should be compared with the corresponding stochastically scale-similar fBm results (albeit for $D \equiv 1.5$) in figure 5(a). It is immediately evident that the local dimension signature $D_2(\epsilon)$ at lengthscales ϵ between the viscous and scalar diffusion scales in these two-dimensional intersections appears very different from that in figure 5(a). The standard deviations $\sigma = 0.144$ and 0.138 in figures 6(a) and 7(a), respectively, are much larger than the corresponding values in table 2 for fBm sets having the same average dimension and record size. This can be contrasted with the corresponding results from one-dimensional intersections by comparing figures 8(a), 10(a), and 18(a) of Part 1 with their respective fBm counterparts in figures 5(b) and 15 of Part 1. The reasons for this

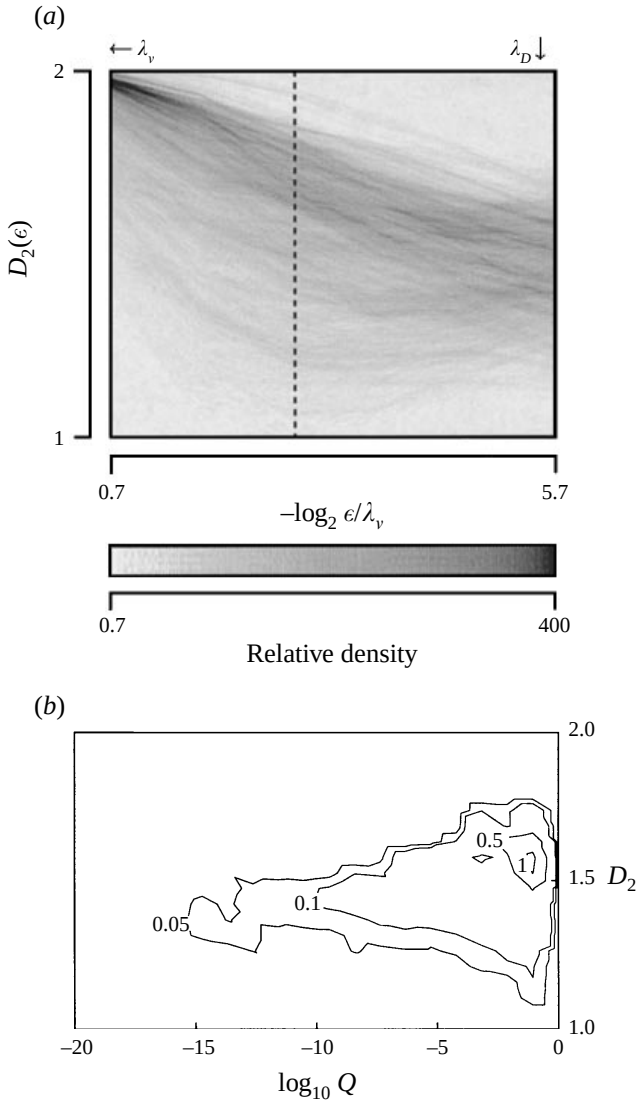

FIGURE 6. (*a*) $D(\epsilon)$ and (*b*) joint Q and $\langle D(\epsilon)\rangle$ signatures obtained from analysis of two-dimensional intersections with the scalar energy dissipation support of data set R0703.

D	$\langle D\rangle$	$\sigma(\langle D\rangle)$
1.1	1.165	0.040
1.2	1.240	0.042
1.3	1.319	0.041
1.4	1.408	0.039
1.5	1.500	0.039
1.6	1.604	0.043
1.7	1.718	0.045
1.8	1.841	0.039
1.9	1.945	0.020

TABLE 2. The D statistics generated from analysis of 9000 two-dimensional fractional Brownian motion sets with varying dimension.

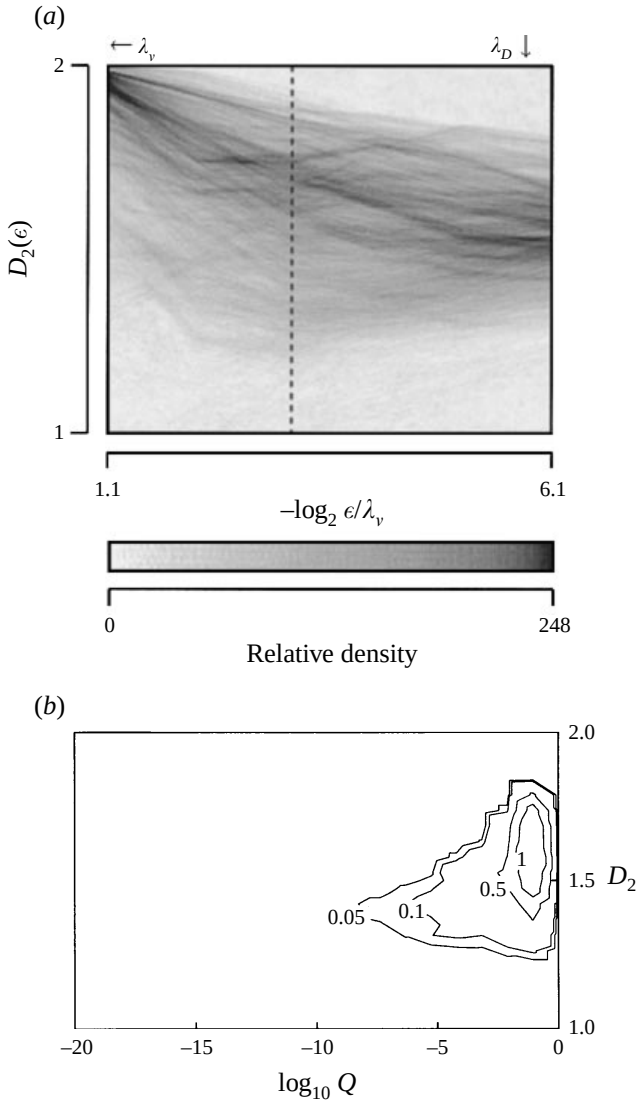

FIGURE 7. (*a*) $D(\epsilon)$ and (*b*) joint Q and $\langle D(\epsilon)\rangle$ signatures obtained from analysis of two-dimensional intersections with the scalar energy dissipation support of data set R0304.

apparent difference between one-dimensional and two-dimensional intersections will become clearer in §6.1 below. Even at this stage, however, close inspection of Region 2 in the present figures 6(*a*) and 7(*a*) reveals that many intersections produce a relatively good asymptotic approach to constant dimension with decreasing lengthscale (ϵ/λ_v), but appear to show a relatively wide range of dimensions.

This latter point is more directly evident in the corresponding joint $\langle D\rangle$ and Q statistics in figures 6(*b*) and 7(*b*) from these same two-dimensional intersections. These should be compared with the corresponding contours for fBm sets over the entire range of dimensions in figure 5(*b*). As indicated in table 3, 49.4% of the intersections in case R0703 and 83.9% of the intersections in case R0304 produced $\langle D\rangle$ and Q values to the right of the 90% contour for fBm sets, and thus were as fractal as 90% of fBm sets

		Two-dimensional results				Three-dimensional results			
		χ support		ζ isosurface		χ support		ζ isosurface	
Data volume	$t/(\lambda_v/u)$	Fractal (%)	$\langle D_2 \rangle$	Fractal (%)	$\langle D_2 \rangle$	$\log_{10} Q$	D_3	$\log_{10} Q$	D_3
R0806039	0.00	28.1	1.37	45.5	1.31	−77.80	2.31	−58.89	2.23
42	2.41	41.2	1.34	42.4	1.28	−36.50	2.25	−52.20	2.20
44	4.02	47.4	1.50	41.6	1.30	−13.70	2.46	−64.19	2.24
47	6.43	66.2	1.60	54.4	1.27	−4.10	2.57	−47.55	2.18
49	8.04	44.1	1.50	28.7	1.28	−6.70	2.45	−54.58	2.19
52	10.45	33.7	1.33	29.3	1.28	−0.78	2.21	−54.34	2.19
55	12.86	49.9	1.31	57.6	1.25	−6.68	2.22	−41.12	2.15
57	14.47	61.2	1.40	77.0	1.27	−0.91	2.31	−29.35	2.16
59	16.08	81.8	1.54	19.6	1.27	−1.33	2.47	−66.97	2.18
62	18.49	96.5	1.67	48.7	1.28	−0.77	2.64	−41.89	2.20
64	20.10	77.5	1.72	71.0	1.30	−2.12	2.71	−25.95	2.20
67	22.51	64.1	1.64	68.0	1.22	−3.13	2.61	−17.00	2.10
69	24.11	85.9	1.64	59.5	1.26	−2.66	2.61	−45.55	2.17
Average	—	59.8	1.50	79.4	1.28	—	2.45	—	2.18
R0703034	0.00	91.5	1.56	56.6	1.27	−0.70	2.51	−52.54	2.19
37	1.45	71.5	1.60	27.3	1.27	−3.62	2.57	−74.25	2.18
39	2.42	28.4	1.54	49.0	1.26	−7.76	2.51	−68.54	2.17
42	3.87	18.5	1.35	22.7	1.34	−50.70	2.30	−88.78	2.28
44	4.84	11.2	1.50	18.0	1.35	−16.30	2.46	−51.13	2.28
47	6.29	24.8	1.44	15.3	1.35	−27.80	2.38	−81.74	2.30
49	7.26	27.4	1.46	16.5	1.34	−18.20	2.40	−84.16	2.28
52	8.71	66.4	1.60	13.7	1.30	−3.78	2.57	−97.75	2.23
54	9.68	91.3	1.68	20.5	1.31	−1.31	2.66	−91.59	2.24
57	11.13	62.0	1.46	41.0	1.26	−2.14	2.42	−37.59	2.17
59	12.10	37.1	1.31	73.4	1.22	−3.62	2.18	−5.95	2.10
62	13.55	63.1	1.35	30.5	1.22	−2.81	2.27	−9.20	2.08
Average	—	49.4	1.49	32.1	1.29	—	2.44	—	2.21
R0304037	0.00	99.3	1.73	69.1	1.23	−1.08	2.71	−23.71	2.11
39	0.63	97.3	1.70	57.0	1.23	−0.60	2.67	−18.25	2.10
42	1.58	98.2	1.74	41.6	1.20	−0.07	2.72	−3.24	2.07
44	2.21	55.4	1.42	53.0	1.17	−0.37	2.36	−25.46	2.08
47	3.15	91.6	1.57	55.6	1.27	−4.19	2.52	−43.64	2.17
49	3.78	98.0	1.58	56.2	1.23	−2.77	2.54	−53.15	2.14
52	4.73	82.7	1.53	80.0	1.25	−1.27	2.46	−34.03	2.15
54	5.36	90.6	1.50	66.2	1.23	−1.49	2.45	−36.94	2.12
57	6.31	55.8	1.41	53.5	1.26	−0.11	2.31	−15.87	2.14
59	6.94	60.6	1.37	58.5	1.25	−0.71	2.24	−5.27	2.12
62	7.89	83.8	1.49	58.0	1.29	−6.84	2.44	−47.42	2.20
64	8.52	75.2	1.56	52.8	1.29	−6.55	2.52	−58.66	2.21
67	9.46	96.8	1.62	37.9	1.28	−2.42	2.58	−80.40	2.20
Average	—	83.9	1.55	56.9	1.24	—	2.50	—	2.14

TABLE 3. Results by data volume from two- and three-dimensional analyses of intersections with the scalar dissipation support and scalar isosurface data.

having the same record size. These percentages should be compared with the corresponding results from one-dimensional intersections, where 90% of records having similar length were found to be as fractal as 99% of fBm sets (see table 5 of Part 1; for the 90% contour used in the present study, 78% of one-dimensional

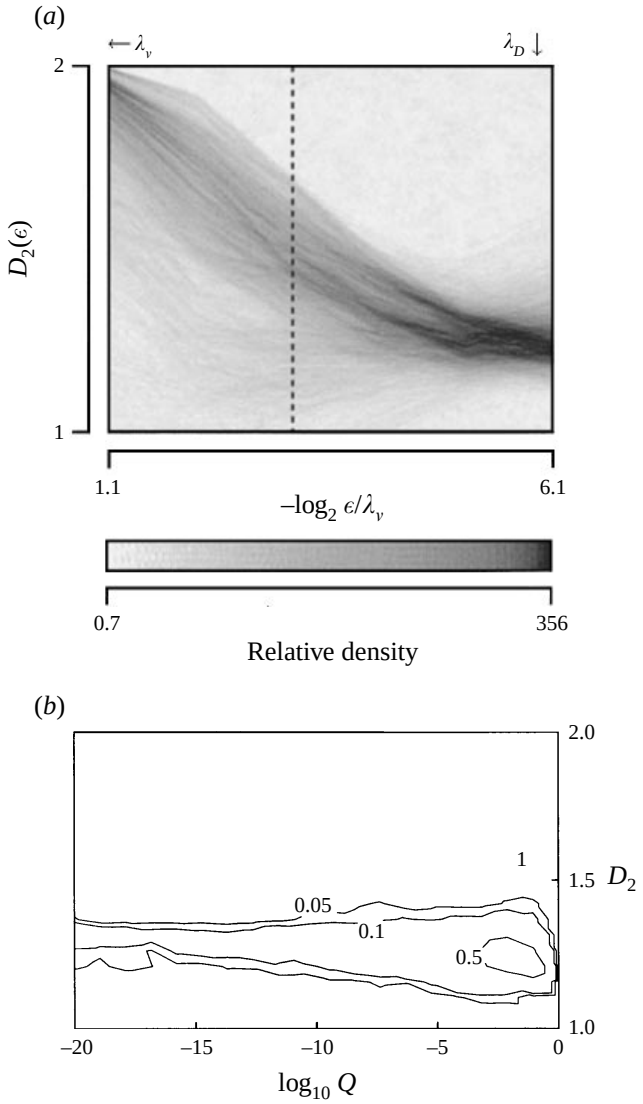

FIGURE 8. (*a*) $D(\epsilon)$ and (*b*) joint Q and $\langle D(\epsilon) \rangle$ signatures obtained from analysis of two-dimensional intersections with the average scalar isosurface of data set R0703.

intersections in Part 1 were as fractal as fBm sets). Note that the different percentages obtained for cases R0703 and R0304 appear consistent with the $D_2(\epsilon)$ results in figures 6(*a*) and 7(*a*). Moreover, as can be seen in table 3, within the results obtained individually for each of the volumes analysed in each case, there are instances of consistent and rather large variations with time in the percentage of intersections found to be as fractal as fBm sets. The reason for these variations will become clear in §6.1, though even here the time variations in table 3 are potentially indicative of intermittent non-fractal inclusions advecting through the measurement volume, which interrupt scale similarity in intersections that pass through them.

As was also apparent in the $D_2(\epsilon)$ results in figures 6(*a*) and 7(*a*), the joint $\langle D \rangle$ and Q statistics in figures 6(*b*) and 7(*b*) show a relatively wide range of dimensions. The

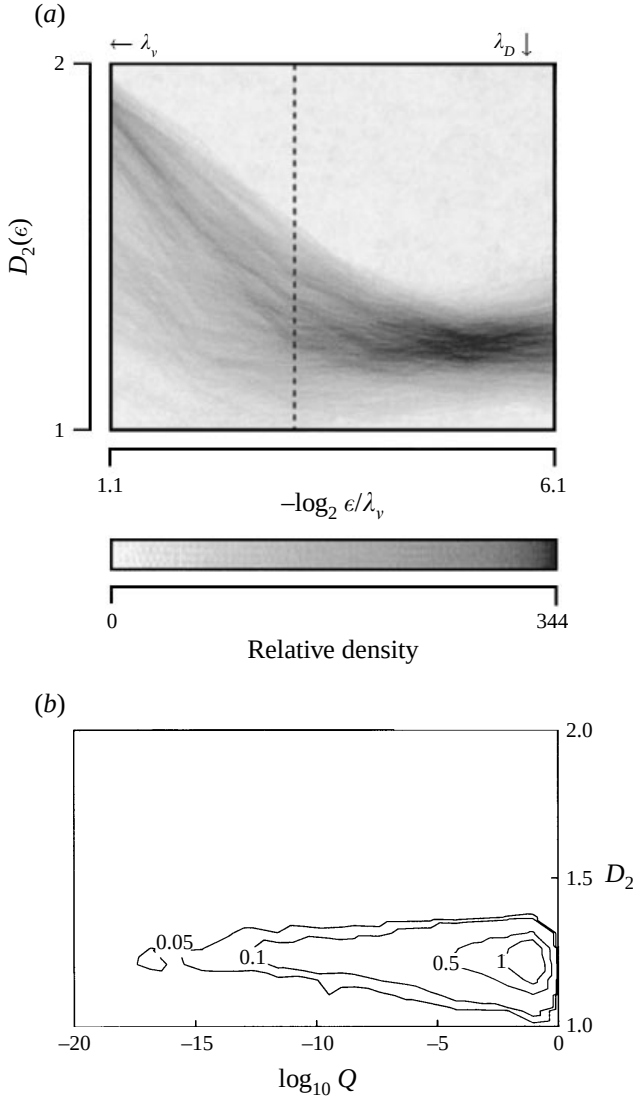

FIGURE 9. (*a*) $D(\epsilon)$ and (*b*) joint Q and $\langle D(\epsilon)\rangle$ signatures obtained from analysis of two-dimensional intersections with the average scalar isosurface of data set R0304.

overall average dimensions found for cases R0703 and R0304 in these figures are $D_2 = 1.49$ and 1.55, respectively. These are lower than would be expected from the method of intersections based on the $D_1 = 0.66$ result from one-dimensional intersections in Part 1. However, figures 6(*b*) and 7(*b*) show that the average dimension at each Q rises with increasing Q values (corresponding to increasingly fractal scale similarity). It is only as $\log_{10} Q \to 0$ that D_2 approaches the value 1.66 expected from the $D_1 = 0.66$ result in Part 1 by the relation $D_n = D-(3-n)$ among codimensions of uniform fractal sets. The reasons for this apparent failure of the method of intersections when applied to the overall average dimensions will become clear in §6.1, where it will be seen that the presence of non-fractal inclusions fully reconciles the present results with the corresponding one-dimensional results from Part 1.

4.3. *Scalar isosurface intersections*

In this section, results analogous to those for the scalar dissipation support geometry in §4.2 are presented to assess scale similarity in scalar isosurface geometries. Only isosurfaces corresponding to the mean scalar value are examined here, since this choice yields the greatest number of isosurface crossings and thus the largest possible statistical sample available from the data. Effects of varying the scalar isosurface value were examined in Part 1.

Figures 8 and 9 present results for the scale-similarity properties of scalar isosurfaces for the same two cases (R0703 and R0304) considered in figures 6 and 7. Each of these figures represents ensemble statistics collected from the same nearly 10000 individual two-dimensional intersections through the same typically thirteen 256^3 spatial data volumes examined in §4.2 (see table 3). However, these intersections are now of the type in figures 1(*a*) and 2(*a*), and the volumes are of the type in figures 3(*a*) and 4(*a*). The range of lengthscales examined again spans from the scalar diffusion scale λ_D to the viscous diffusion scale λ_ν.

Figures 8(*a*) and 9(*a*) give the ensemble $D_2(\epsilon)$ results for each of these two cases, and figures 8(*b*) and 9(*b*) show the corresponding joint $\langle D \rangle$ and Q statistics for the same intersections. The former should be compared with the corresponding results for stochastically scale-similar fBm sets, as given for $D \equiv 1.5$ in figure 5(*a*). The $D_2(\epsilon)$ results in figures 8(*a*) and 9(*a*) may appear to better asymptote to constant dimension with decreasing scale size than did the corresponding results for the dissipation support in figures 6(*a*) and 7(*a*). However, this can be determined more directly in the corresponding joint $\langle D \rangle$ and Q statistics in figures 8(*b*) and 9(*b*) for these same intersections. Those results should be compared with the probability contours from fBm gauge sets for dimensions $1 < D < 2$ in figure 5(*b*). It is apparent that relatively few of these two-dimensional intersections over this range of scales are as fractal as fBm sets having the same record size, with most intersections giving Q values much lower than corresponding fBm sets. As indicated in table 3, only 32.1% of the intersections in case R0703 and 56.9% of the intersections in case R0304 produced $\langle D \rangle$ and Q values to the right of the 90% contour for fBm sets.

Whereas the one-dimensional intersections in Part 1 found the scalar isosurface geometry over the inner range of scales to be at least approximately representable by fBm sets with $D_1 \approx 0.48$, the present results suggest dimensions $D_2 \approx 1.28$ much lower than the value $D_2 = 1.48$ that would be expected from the method of intersections. This apparent failure of the method of intersections is consistent with the finding in §4.2, and will also be seen in the three-dimensional results in §5. In §6.1 this will be seen to result from a fundamentally non-fractal structure in the scalar isosurfaces at scales near λ_D.

5. Three-dimensional intersections

This section presents corresponding results for scale similarity in three-dimensional intersections through scalar isosurface sets and scalar dissipation support sets for each of the cases listed in table 1. Criteria based on stochastically self-similar three-dimensional fBm gauge sets, constructed from superpositions of one-dimensional fBm sets, are developed in §5.1, with results for geometric scale-similarity properties of the dissipation support given in §5.2 and for the scaling properties of scalar isosurfaces given in §5.3.

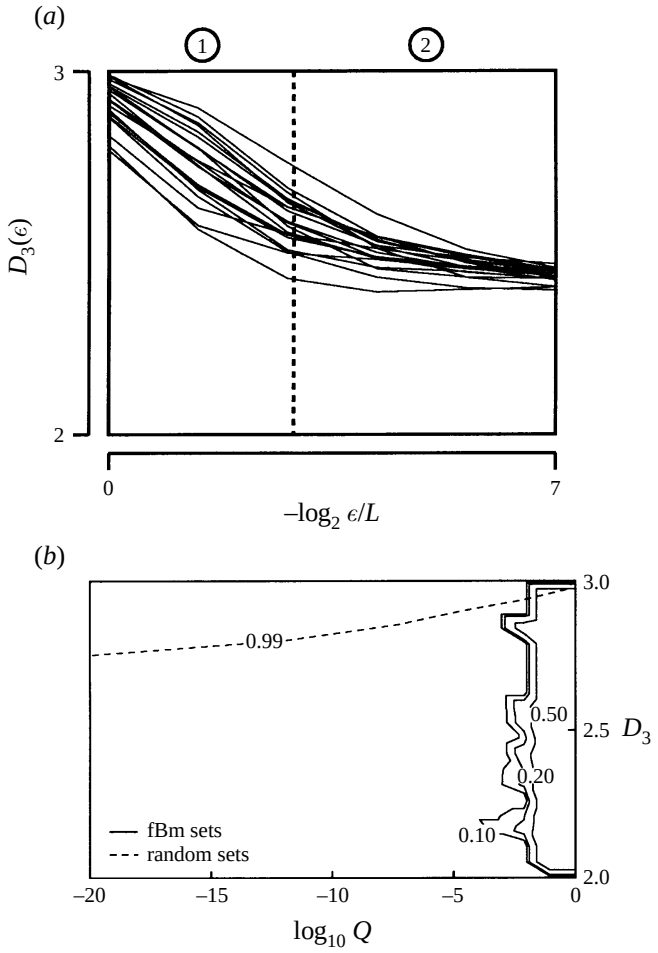

FIGURE 10. (*a*) $D(\epsilon)$ results from fractional Brownian motion sets with $D = 2.5$ and (*b*) the corresponding fractal criterion developed from analysis of many three-dimensional fractional Brownian motion sets.

5.1. *Three-dimensional calibrations*

Three-dimensional calibrations were performed with fBm gauge sets having dimensions $2 < D < 3$ in increments of $\Delta D = 0.1$. As an example, results for the $D(\epsilon)$ signatures of 20 individual realizations of three-dimensional (256^3) fBm sets, each having $D = 2.5$, are presented in figure 10(*a*). These should be compared with the corresponding results for two-dimensional fBm sets in figure 5(*a*) and one-dimensional fBm sets in figure 5(*b*) of Part 1. As in §4.1 and in Part 1, the standard deviation σ in $D(\epsilon)$ over Region 2 and the average value $\langle D(\epsilon) \rangle$ provide a means for assessing if a given three-dimensional set displays scale similarity as fractal as an fBm set having the same average dimension over the same range of scales. Results obtained from such calibrations for three-dimensional fBm sets over the range of dimensions $2 < D < 3$ are given in table 4.

Joint $\langle D \rangle$ and Q statistics from the three-dimensional fBm sets above are presented in figure 10(*b*), which can be compared with the corresponding results for two-dimensional fBm sets in figure 5(*b*) and for one-dimensional fBm sets in figure 6(*b*) of Part 1. The numerical values again denote the fraction of sets producing $\langle D \rangle$ and Q

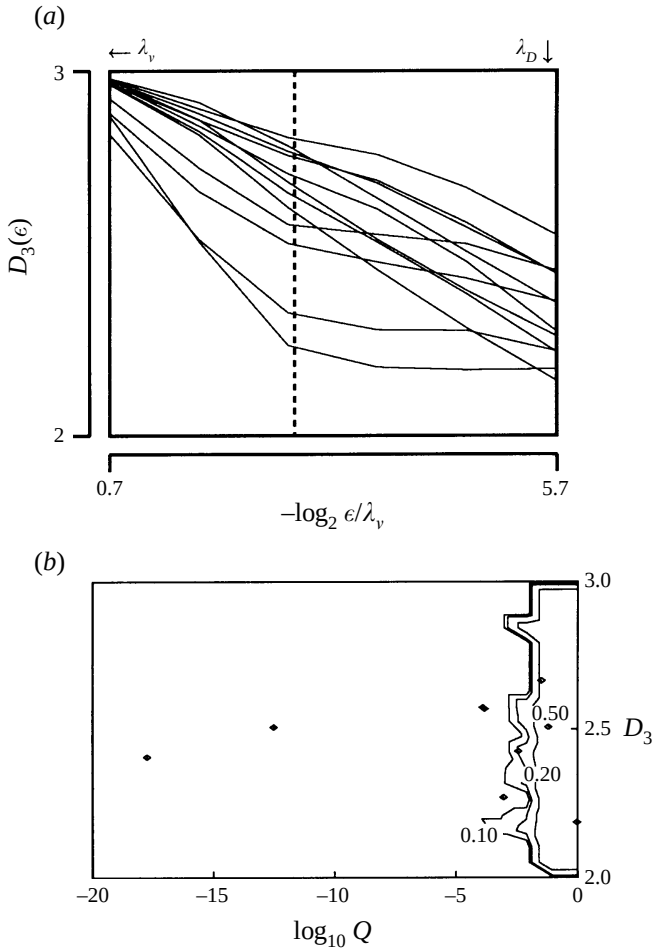

FIGURE 11. (*a*) $D(\epsilon)$ and (*b*) joint Q and $\langle D(\epsilon)\rangle$ signatures obtained from analysis of the dissipation support of the full three-dimensional data volumes of data set R0703.

D	$\langle D\rangle$	$\sigma(\langle D\rangle)$
2.1	2.148	0.023
2.2	2.219	0.025
2.3	2.309	0.019
2.4	2.389	0.030
2.5	2.469	0.029
2.6	2.580	0.029
2.7	2.686	0.037
2.8	2.825	0.038
2.9	2.922	0.021

TABLE 4. The D statistics generated from analysis of 180 three-dimensional fractional Brownian motion sets with varying dimension.

values to the right of each contour. Note that, given the much higher information content in these (256^3) sets, the contour bounding 99% of all random percolation sets in these three-dimensional calibrations lies well beyond the left-hand edge of the plot in figure 10(*b*), corresponding to Q values below 10^{-20}, except very close to the limiting

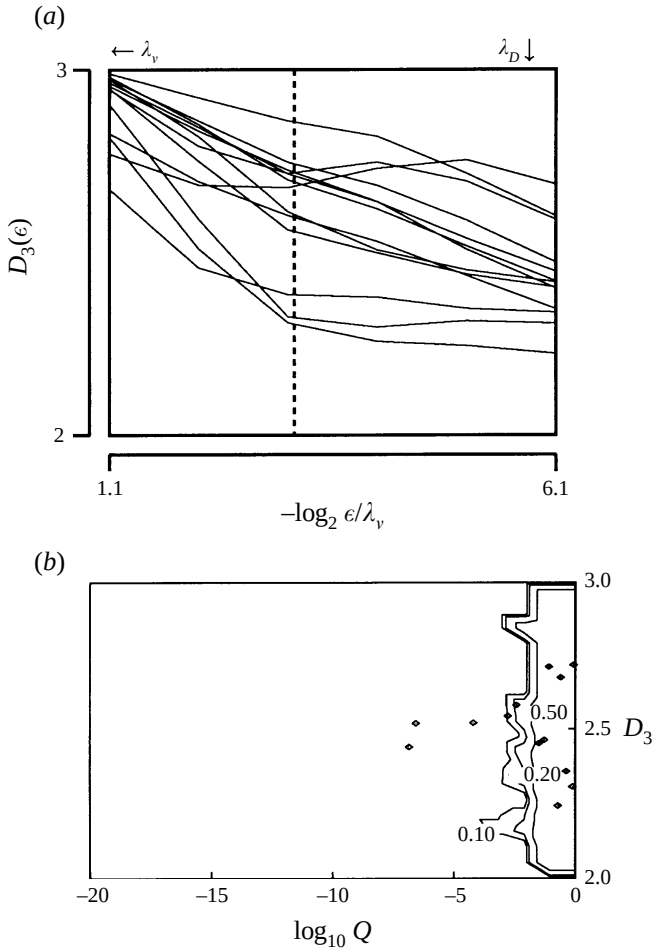

FIGURE 12. (*a*) $D(\epsilon)$ and (*b*) joint Q and $\langle D(\epsilon)\rangle$ signatures obtained from analysis of the dissipation support of the full three-dimensional data volumes of data set R0304.

value $D = 3$. Similarly, the contours bounding essentially all fractal sets are tightly concentrated near the right-hand end of the plot, corresponding to comparatively large Q values. Thus, even more so than for the two-dimensional intersections in §4, in analysing three-dimensional intersections there is a totally unambiguous distinction between fractal and random sets. Indeed unlike the corresponding results for one-dimensional and two-dimensional fBm sets, in these three-dimensional analyses it is effectively possible to define a single Q-value ($\log_{10} Q \approx -3$) to distinguish between fractal and non-fractal scale similarity.

5.2. *Scalar dissipation support intersections*

Figures 11 and 12 show results from three-dimensional analyses of the same thirteen 256^3 spatial data volumes from each of cases R0703 and R0304 for which two-dimensional intersections were analysed in §4. Each of these volumes again spans the range of scales between the scalar diffusion scale λ_D and the viscous diffusion scale λ_ν.

Figures 11(*a*) and 12(*a*) give the emsemble results for the dimension $D_3(\epsilon)$ from the three-dimensional intersections for these two cases, and should be compared with the results for stochastically scale-similar fBm sets with $D \equiv 2.5$ in figure 10(*a*). Consistent

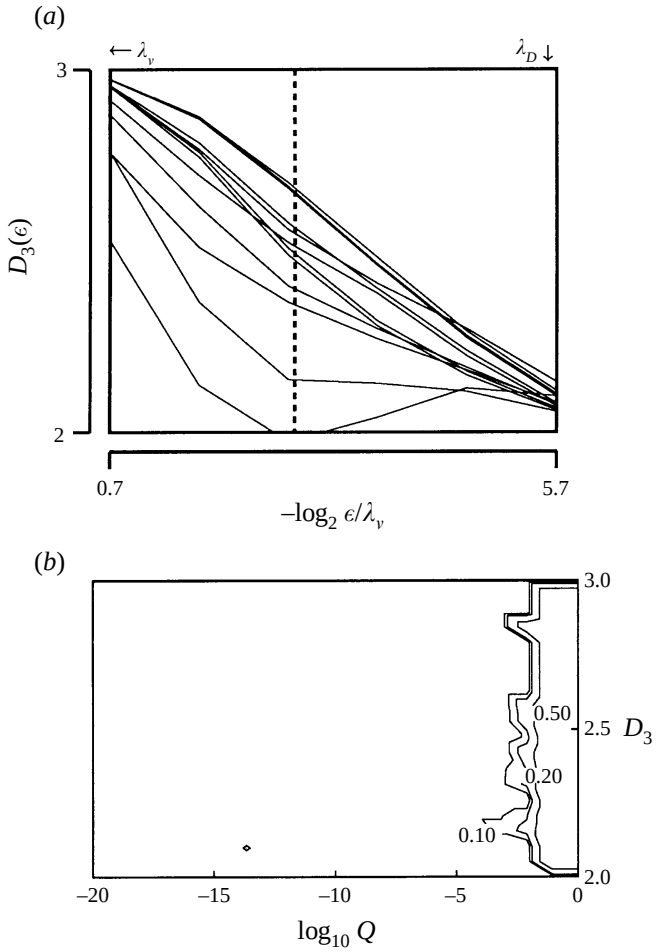

FIGURE 13. (*a*) $D(\epsilon)$ and (*b*) joint Q and $\langle D(\epsilon)\rangle$ signatures obtained from analysis of the average scalar isosurface of the full three-dimensional data volumes of data set R0703.

with what was found from two-dimensional intersections in §4, the local dimension signature $D_3(\epsilon)$ at lengthscales ϵ between the viscous and scalar diffusion scales in these three-dimensional intersections appears very different from that in figure 10(*a*). The corresponding joint $\langle D\rangle$ and Q values are given in figures 11(*b*) and 12(*b*) for these same three-dimensional intersections, where the probability contours for stochastically self-similar fBm sets from figure 10(*b*) are also shown for comparison. Owing to the fact that no more than 13 volumes were analysed in each case, the resulting joint $\langle D\rangle$ and Q values are shown as points rather than probability contours. Table 3 shows the time variation in the D_3 and $\log_{10} Q$ values for each of the scalar dissipation volumes analysed in each of the three cases considered, where a very clear variation with time in the $\log_{10} Q$ values can be seen.

Note that only 4 of the 12 volumes (33%) from case R0703 in figure 11(*b*) show scale similarity throughout the entire three-dimensional (256^3) volume comparable with the fBm gauge sets. This should be compared with the 49.4% and 74.7% values obtained, respectively, from two-dimensional and one-dimensional intersections through the volumes analysed from case R0703. Similarly, for case R0304, 10 out of

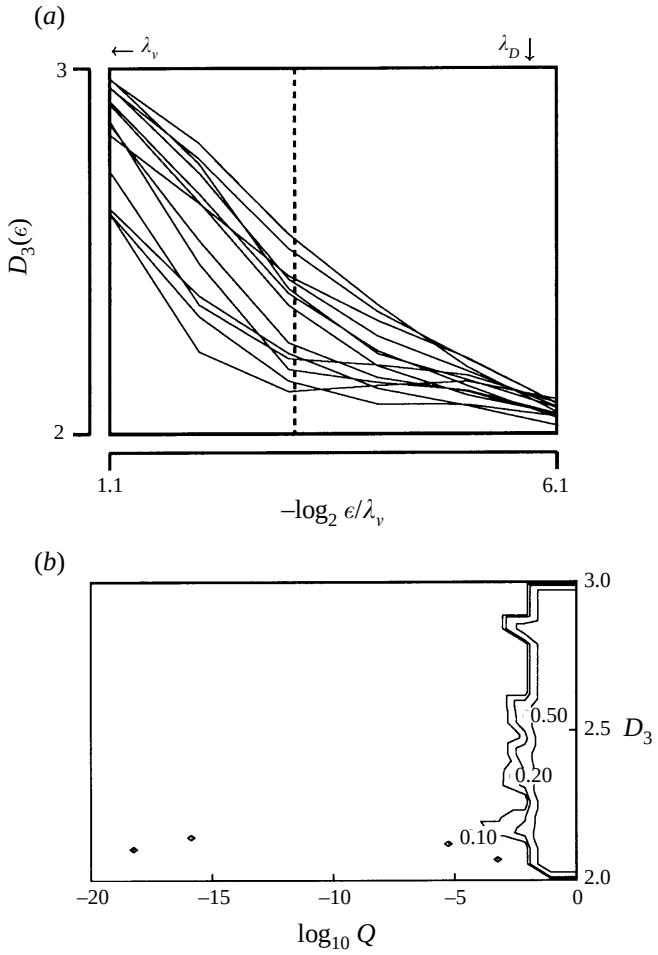

FIGURE 14. (*a*) $D(\epsilon)$ and (*b*) joint Q and $\langle D(\epsilon)\rangle$ signatures obtained from analysis of the average scalar isosurface of the full three-dimensional data volumes of data set R0304.

13 intersections (77%) in figure 12(*b*) show scale similarity throughout the entire (256^3) volume consistent with fBm sets, compared with the 83.4% and 83.9% values obtained, respectively, from two-dimensional and one-dimensional intersections. For those volumes having $\log_{10} Q \geqslant -3$ (i.e. showing fractal scale similarity), the resulting average dimension in figures 11(*b*) and 12(*b*) is $D_3 \approx 2.49$, in relatively good agreement with the value $D_2 \approx 1.52$ from the two-dimensional intersections in §4.2.

The pattern that is suggested by these results is one of a decreasing percentage of intersections showing uniform scale similarity consistent with fBm sets as the intersection dimension increases. The reasons for this will become fully evident in §6.1 below, but even at this stage it is apparent that this would be consistent with the presence of non-fractal inclusions embedded in an otherwise fractal background structure. The fraction of intersections that would pass through such inclusions, and thus show interrupted fractal scale similarity, would increase as the intersection dimension increases, leading to a decreasing percentage of intersections showing uniform scale-similarity as the intersection dimension increases. This in turn would lead to the observed decrease with intersection dimension in the fraction of intersections

found to be fractal. Note that this would be consistent as well with the time variations seen in the $\log_{10} Q$ values in table 3.

5.3. *Scalar isosurface intersections*

Figures 13 and 14 present corresponding results for scalar isosurfaces for the same cases considered in §5.2 above and in §4. Figures 13(*a*) and 14(*a*) give ensemble $D_3(\epsilon)$ results for the scalar isosurface geometries from cases R0703 and R0304. These should be compared with the $D(\epsilon)$ signature for stochastically scale-similar fBm sets, shown for $D \equiv 2.5$ in figure 10(*a*). For the same reasons as noted in §4.3, these results do not appear to be consistent with the scale similarity embodied in fBm sets. Instead they show an approach to $D_3(\epsilon) \to 2$ as the scale $\epsilon \to 0$, consistent with the expected cutoff scale at λ_D, below which scalar isosurfaces should appear as topologically simple planar surfaces. However, even at scales well above λ_D, the results in figures 13(*a*) and 14(*a*) do not show any consistency with fractal scale similarity.

The joint $\langle D \rangle$ and Q values for these same three-dimensional intersections are given in table 3 and by the symbols in figures 13(*b*) and 14(*b*), along with the probability contours for the fBm gauge sets from figure 10(*b*). As in §5.2, the joint $\langle D \rangle$ and Q values are shown here as points rather than probability contours. Note that, in both cases, none of the volumes produced Q values large enough to indicate scale similarity throughout the entire three-dimensional (256^3) volume consistent with 90% of all fBm sets ($\log_{10} Q > -3$). Indeed most of the points in figures 13(*b*) and 14(*b*) are well beyond the left-hand edge of the plot, indicating manifestly non-fractal scaling. This should be contrasted with the corresponding results in figures 11(*b*) and 12(*b*) for the scalar dissipation support in the same volumes, which showed clear evidence for fractal scale similarity in many of the volumes over the same range of length scales. Moreover, from figures 13(*b*) and 14(*b*) the resulting average dimension gives $D_3 \approx 2.17$ for these three-dimensional intersections through isoscalar surfaces, whereas the two-dimensional intersections in §4.3 gave $D_2 \approx 1.28$ and the one-dimensional intersections in Part 1 gave $D_1 \approx 0.48$. This failure of the relation $D_n = D-(3-n)$ among codimensions is a further indication for lack of uniform fractal scale similarity in the scalar isosurface fields over this range of lengthscales.

This also establishes a clear trend with increasing intersection dimension, though one that is different in important ways from that seen in §5.2 for the scalar dissipation support geometry. For scalar isosurfaces, the one-dimensional intersections in Part 1 showed roughly 85% of 256-point intersections over the inner range of scales between (λ_D, T_D) and (λ_ν, T_ν) to be as fractal as fBm sets having the same record length (though for scales between (λ_D, T_D) and (δ, T_δ) only 2.6% of intersections appeared consistent with fractal scale similarity). In contrast, the less ambiguous assessment in §4.3 based on two-dimensional intersections over the inner range of scales between λ_D and λ_ν showed only 56% of 256^2 intersections to be as fractal as fBm sets. The even more definitive three-dimensional 256^3 intersections over the same range of scales showed that no scalar isosurface sets were as fractal as fBm sets. Given all of the above evidence, it must be concluded that scalar isosurfaces do not display fractal scale similarity over the inner range of scales, and instead show an approach to classical, topologically simple, two-dimensional surfaces consistent with a cutoff near λ_D.

6. Local scale similarity and non-fractal inclusions

Results in §§4 and 5 from two- and three-dimensional intersections through scalar dissipation support sets over the inner range of scales gave strong evidence for

stochastic fractal scale similarity. However, these same results also showed indications of possible intermittent non-fractal regions within the measurement volume. Indirect evidence for such regions was found in the time variations in table 3 of the fraction of two- and three-dimensional intersections displaying uniform fractal scale-similarity, and in the variation with intersection dimension n of the fraction of one-, two-, and three-dimensional intersections found to show fractal scale-similarity, as well as in the failure of the relation among codimensions D_n from the method of intersections when applied to simple average dimensions.

The notion of regions of non-fractal scaling in turbulent flows is not entirely new. In chaotic flows, isolated regions of non-fractal scaling often associated with KAM islands or tubes have been well-documented both experimentally and analytically (Everson & Screenivasan 1992; Kusch & Ottino 1992; Ottino *et al.* 1992). Fluid in these regions does not experience the same multiplicative stretching and folding that operates on the majority of the fluid, and therefore lacks the fractal scaling found in the remainder of the flow. Though similarities between such chaotic flows and turbulent flows are currently tenuous at best, it is possible that structures similar to such KAM regions might be present in turbulent flows. Recent work by Vassilicos & Hunt (1991) has postulated the presence of power-law vortex roll-up regions which produce the fractal signature in the scalar isosurface fields of turbulent flows measured by Sreenivasan & Meneveau (1986) and Sreenivasan, Ramshankar & Meneveau (1989) without actually being fractals. However, Everson & Sreenivasan (1992) contend that these vortex roll-up regions obey logarithmic scaling instead of the power-law scaling proposed by Vassilicos & Hunt, and thus do not affect the fractal structure of the scalar isosurface fields.

6.1. *Non-fractal inclusions*

If non-fractal inclusions are present in these data, then intersections passing through them would presumably have their fractal scale similarity interrupted, or at least altered, and thus fail to meet the present objective criteria for fractal scaling. This would explain the observed reduction with increasing intersection dimension n in the percentage of intersections found to demonstrate fractal scaling. Note that if every three-dimensional volume of scale L^3 containing a sufficiently large inclusion (say of scale l^3) fails to show fractal scaling, then roughly $1-(l/L)$ of all two-dimensional intersections through the same volumes would miss the inclusion and still give fractal scaling, while $1-(l/L)^2$ of all one-dimensional intersections would miss the inclusion and give fractal scaling. Letting P_0 denote the fraction of all volumes free of such inclusions, the resulting fraction $P_F^{(n)}$ of all n-dimensional intersections that still show fractal scaling would be given by

$$P_F^{(n)} = P_0 + (1-P_0)\left[1-\left(\frac{l}{L}\right)^{(3-n)}\right]. \tag{1}$$

Since $P_0 \equiv P_F^{(3)}$, the typical inclusion scale can then be estimated as

$$\left(\frac{l}{L}\right) = \left[\frac{1-P_F^{(n)}}{1-P_F^{(3)}}\right]^{1/(3-n)}. \tag{2}$$

Using values of $P_F^{(n)}$ from §4.2, §5.2, and from Part 1 (for the 90% contour in the joint $\langle D\rangle$ and Q results given there), as well as the values of L for each case (see figures 2 and 3), produces the inclusion scale estimates (l/L) from (2) given in table 5. Note that

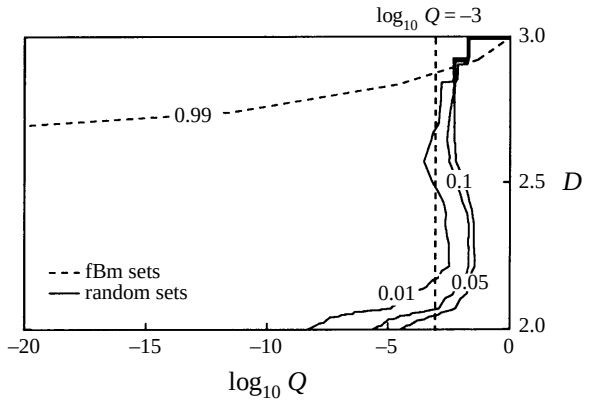

FIGURE 15. Fractal criterion developed for the 64^3 local scale similarity analysis.

Data volumes	Fractal (%) One-dimensional intersections	Two-dimensional intersections	Three-dimensional intersections	$[l/\lambda_\nu]_{1,3}$	$[l/\lambda_\nu]_{2,3}$
R0806	76.6	59.8	38.5	0.23	0.25
R0703	74.7	49.4	33.3	0.27	0.33
R0304	83.9	83.4	76.9	0.47	0.41

TABLE 5. Summary of the fraction of intersections through the dissipation support that were found to be fractal. Included are estimates of the size of the non-fractal inclusions obtained from these data.

within each case the values obtained are rather consistent. The variations between cases may not be surprising in view of the relatively short time span of each case (see table 3). Nevertheless, all the cases considered suggest values for (l/λ_ν) in the range from $\frac{1}{4}$ to $\frac{1}{2}$. While these estimates must be viewed as extremely crude, the agreement among them is strong enough to lend some support to the underlying physical hypothesis that the observed variations in $P_F^{(n)}$ with intersection dimension n and with time may be due to such non-fractal inclusions.

6.2. *Three-dimensional* (64^3) *calibrations*

To investigate the possible presence of such non-fractal inclusions in these data, the same fractal assessment criteria used throughout this study (see §3) were extended to smaller (64^3) three-dimensional volumes to allow point-by-point evaluation of the local goodness-of-fit parameter Q and the dimension D within the interior of each of the three-dimensional (256^3) spatial data volumes analysed in §§4 and 5. The extension to such smaller three-dimensional volumes only required recalibrating the joint $\langle D \rangle$ and Q statistics using 64^3 fBm sets in precisely the same way as was done for 256^3 volumes in §5.1. In this case, scale similarity is evaluated over the range of lengthscales from $0.43\lambda_D$ to $1.7\lambda_D$. The results of this procedure are shown in figure 15, which is analogous to the result for 256^3 fBm sets presented in figure 10(*b*). Note that the cumulative probability contours in figure 15 are nearly as compact as those for the corresponding 256^3 calibrations volumes in figure 10(*b*), except at dimensions very

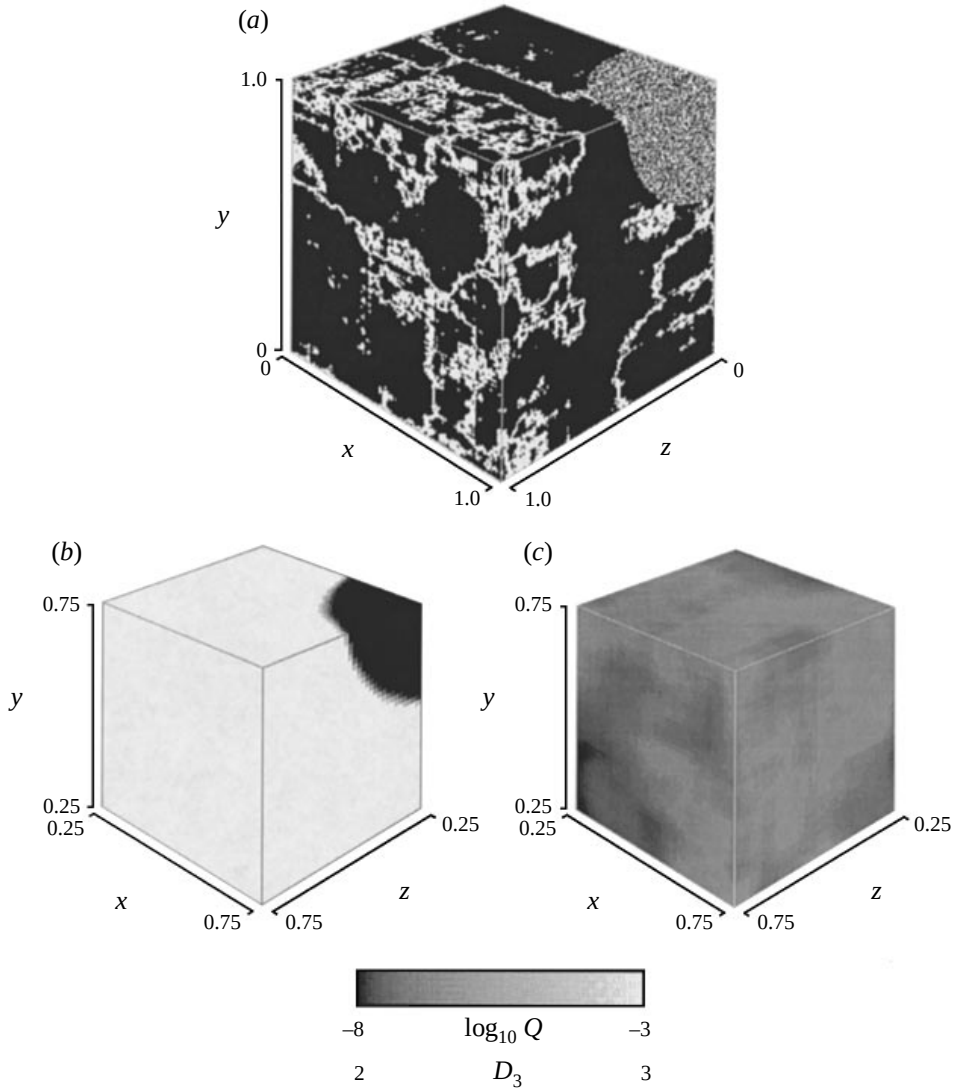

FIGURE 16. (*a*) Local (64^3) scale-similarity results from a three-dimensional fractional Brownian motion set with a non-fractal random spherical insert. The non-fractal insert produces extremely low Q values in (*b*) but does not produce large variations in the D results in (*c*).

close to 2. This allows definition of a threshold Q value at $\log_{10} Q = -3$ effectively separating fractal and non-fractal sets, and containing 90 % of all the 64^3 fBm gauge sets.

Figure 16 demonstrates the ability of this local scale-similarity criterion to discriminate between locally fractal and non-fractal regions. Figure 16(*a*) shows a three-dimensional 256^3 stochastically fractal fBm level-crossing set with dimension $D \equiv 2.5$, constructed with a spherical inclusion centred at the upper right-hand corner within which non-fractal random percolation scaling applies. Analysing 64^3 sub-volumes contained within the original 256^3 set using this criterion produces the local values of the fractal goodness-of-fit parameter $Q(\boldsymbol{x}, t)$ shown in figure 16(*b*) and the

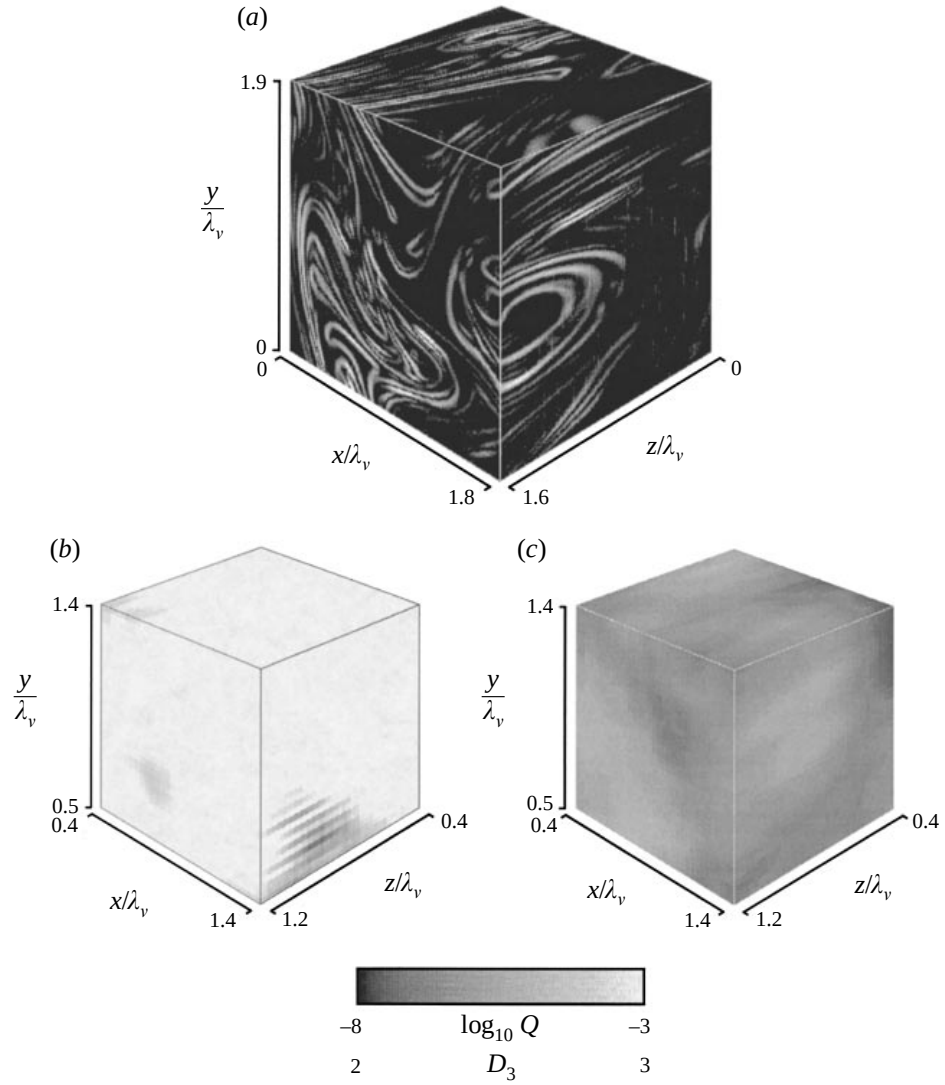

FIGURE 17. (*a*) Local (64^3) scale-similarity results for the dissipation support in the three-dimensional data volume R0304037, which was found to be fractal in §5.2. Only small regions of slightly non-fractal Q values can be seen in (*b*), while the D values in (*c*) remain relatively constant throughout the data volume.

dimension values $D_3(\boldsymbol{x}, t)$ in figure 16(*c*). It is readily apparent that the technique unequivocally identifies the non-fractal spherical inclusion by the exceedingly low Q values at the upper right-hand corner of the cube. The corresponding dimension D_3 values vary somewhat throughout the volume owing to the stochastic nature of the original fractal set, and as usual are slightly lower than the true dimension $D = 2.5$. The variations in D_3 values in figure 16(*c*) set the standard for declaring the sets in §§6.3 and 6.5 to have a single true dimension. More importantly, the Q values in both the fractal and non-fractal regions in figure 16(*b*) indicate the threshold for identifying non-fractal inclusions in the sets in §§6.3–6.5.

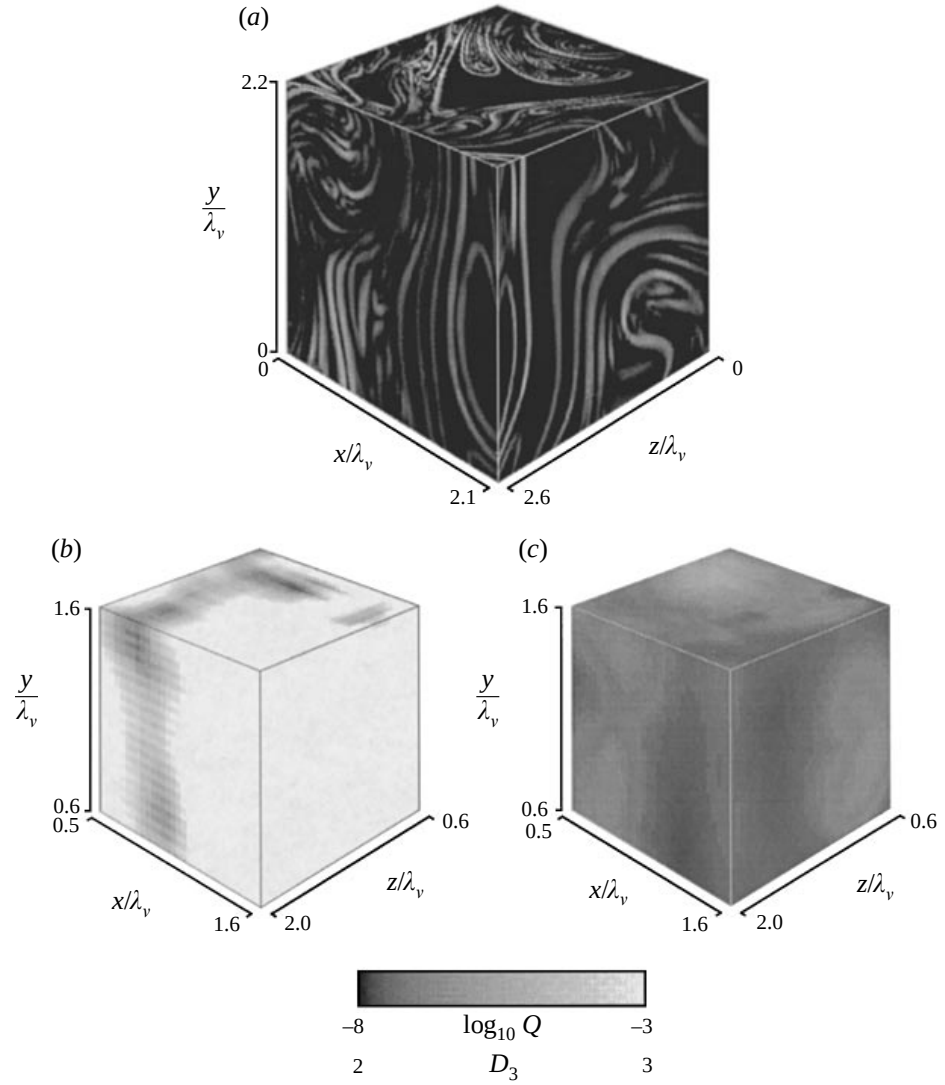

FIGURE 18. (*a*) Local (64^3) scale-similarity results for the dissipation support in the three-dimensional data volume R0703054, which was found to be fractal in §5.2. Only small regions of slightly non-fractal Q values can be seen in (*b*), while the D values in (*c*) remain relatively constant throughout the data volume.

6.3. *Scalar dissipation support intersections*

Based on the success of this local scale-similarity criterion in correctly identifying non-fractal inclusions in a variety of test cases like that in figure 16, this approach was applied to all the volumes analysed in §§4 and 5 to investigate the possible presence of such non-fractal inclusions in these data. Figures 17–19 show results from the local (64^3) scale-similarity analysis for three typical data volumes that were found to be fractal from the full 256^3 analyses in §5.2 and figures 11 and 12. In each figure, part (*a*) shows the corresponding three-dimensional (256^3) scalar dissipation field, part (*b*) the local fractal goodness-of-fit parameter $Q(\boldsymbol{x}, t)$, and part (*c*) the local dimension values

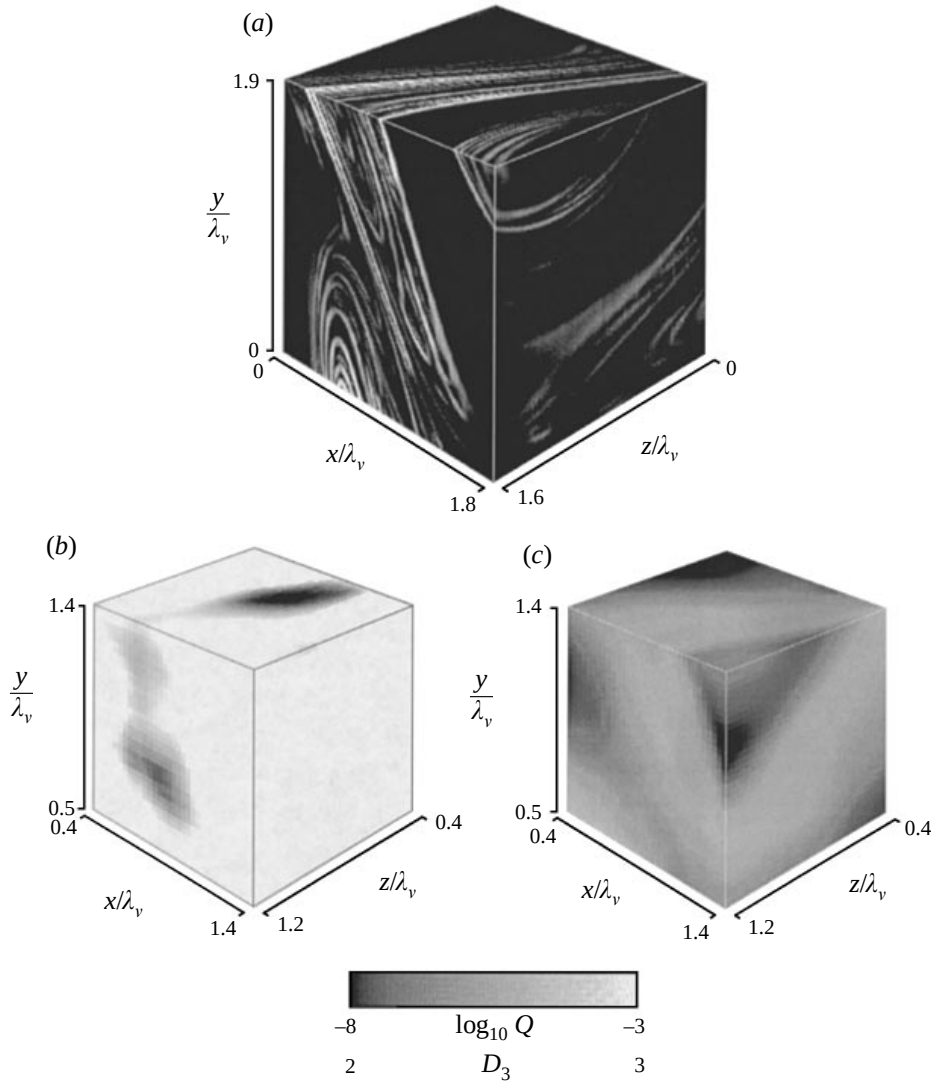

FIGURE 19. (*a*) Local (64^3) scale-similarity results for the dissipation support in the three-dimensional data volume R0304039, which was found to be fractal in §5.2. Only small regions of significantly non-fractal Q values can be seen in (*b*), while the D values in (*c*) remain relatively constant throughout the data volume.

$D_3(\boldsymbol{x}, t)$. Note that, throughout most of the volume, figures 17 and 18 show Q values near or exceeding the 10^{-3} threshold for fractal scaling based on the calibration results in figure 15. Moreover, based on the standard in figure 16(*c*), these volumes also show essentially constant dimensions throughout, with the dimension $\langle D_3 \rangle \approx 2.71$ and 2.66 in figures 17 and 18, respectively. In such volumes, the relation among codimensions D_n appears to be relatively well satisfied. By comparison, figure 19 shows a volume with somewhat larger departures from strict uniform fractal scale-similarity, though it was still found to be fractal in the full 256^3 analyses, with $\log_{10} Q = -0.60$. Nevertheless, figure 19(*b*) shows a small region near the top surface that locally demonstrates significantly non-fractal scale similarity. Putting this relatively small

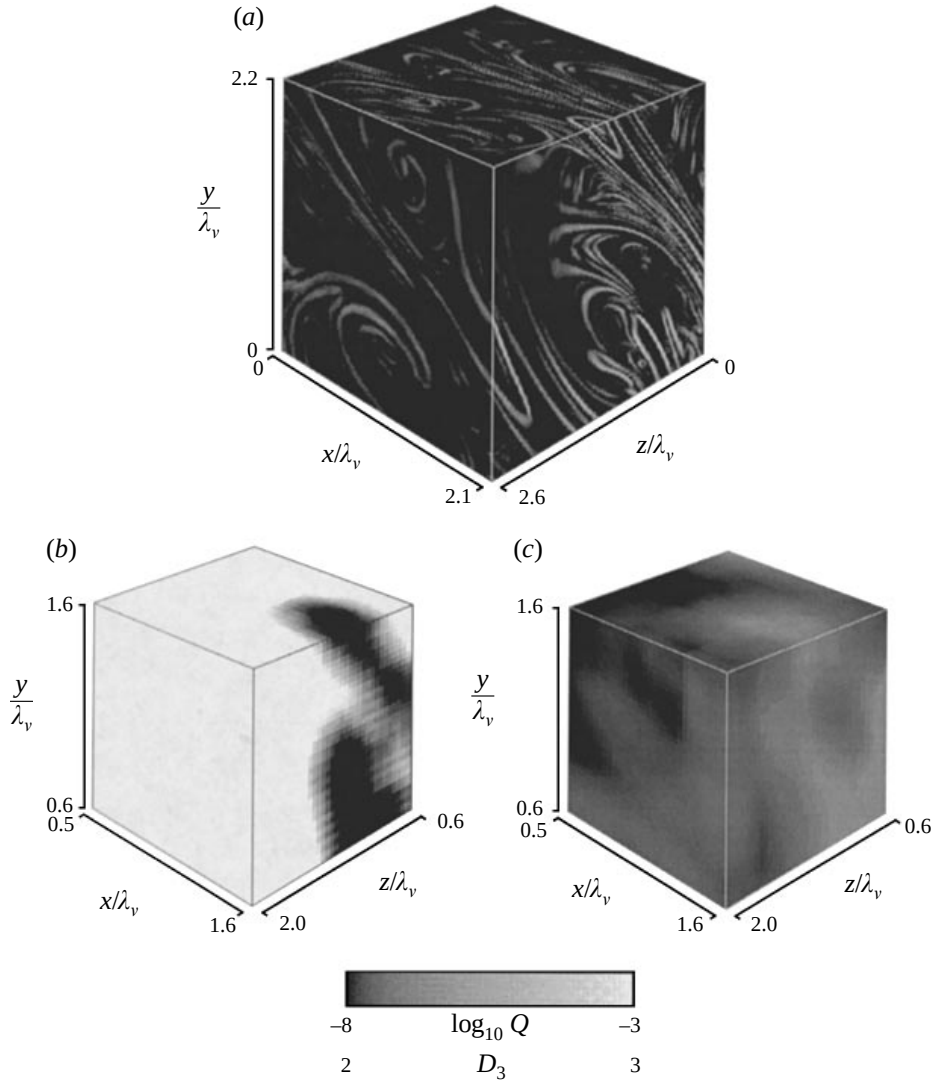

FIGURE 20. (*a*) Local (64^3) scale-similarity results for the dissipation support in the three-dimensional data volume R0703039, which was found to be non-fractal in § 5.2. Large regions of significantly non-fractal Q values can be seen in (*b*).

region of non-fractal scaling aside for the moment, the departures from essentially uniform dimension D_3 in figure 19(*c*) appear to be simply due to voids in the dissipation field over scales that are relatively large in comparison with the 64^3 scale over which the analysis extends. The dimension estimate D_3 obtained on nearly empty boxes is naturally biased toward lower values.

Figures 20–22 show corresponding results for three typical data volumes that were found to be non-fractal in the full 256^3 analyses. In each case, the primary distinguishing feature is the presence of one or more relatively large inclusions within which the scaling is clearly non-fractal, as evidenced by the regions with exceedingly low Q values in part (*b*) of each of these figures. In many cases, these non-fractal inclusions appear to be closely associated with regions where the scalar dissipation

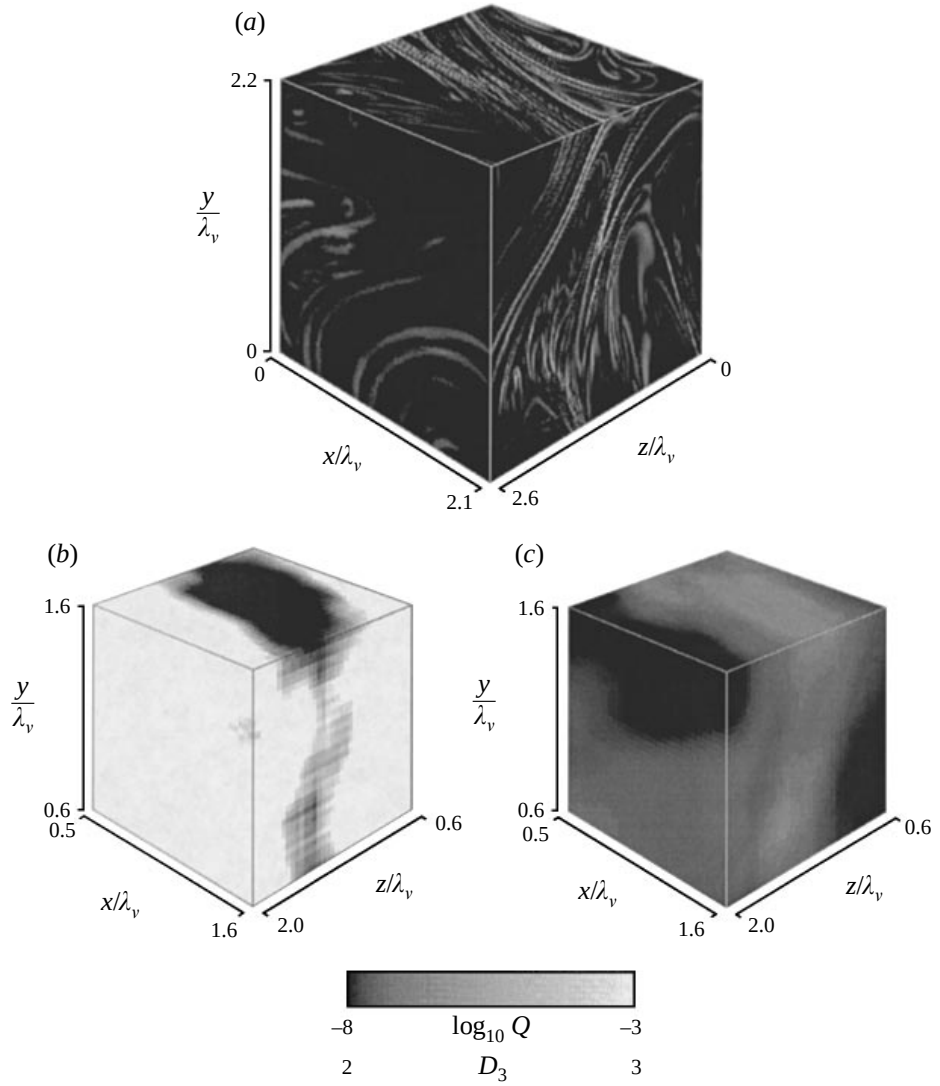

FIGURE 21. (*a*) Local (64^3) scale-similarity results for the dissipation support in the three-dimensional data volume R0703049, which was found to be non-fractal in §5.2. Large regions of significantly non-fractal Q values can be seen in (*b*), which correspond to regions of highly parallel dissipation layers.

layers are tightly packed into nearly parallel structures. The topology of these inclusions varies widely, from roughly spherical to nearly slab-like, as in figure 22, and some cases appear to show more than one inclusion, as in figure 20. However, in each case the characteristic lengthscale of these inclusions is of the order of the viscous diffusion scale λ_ν. This is in at least rough agreement with the crude estimates obtained in §6.1 and table 5.

6.4. *Non-fractal inclusion scale*

Given the clear evidence in §6.3 for non-fractal inclusions in these data, in this section we determine their characteristic lengthscale based on an equivalent spherical model for the inclusions. A natural choice for such a characteristic scale might appear to be

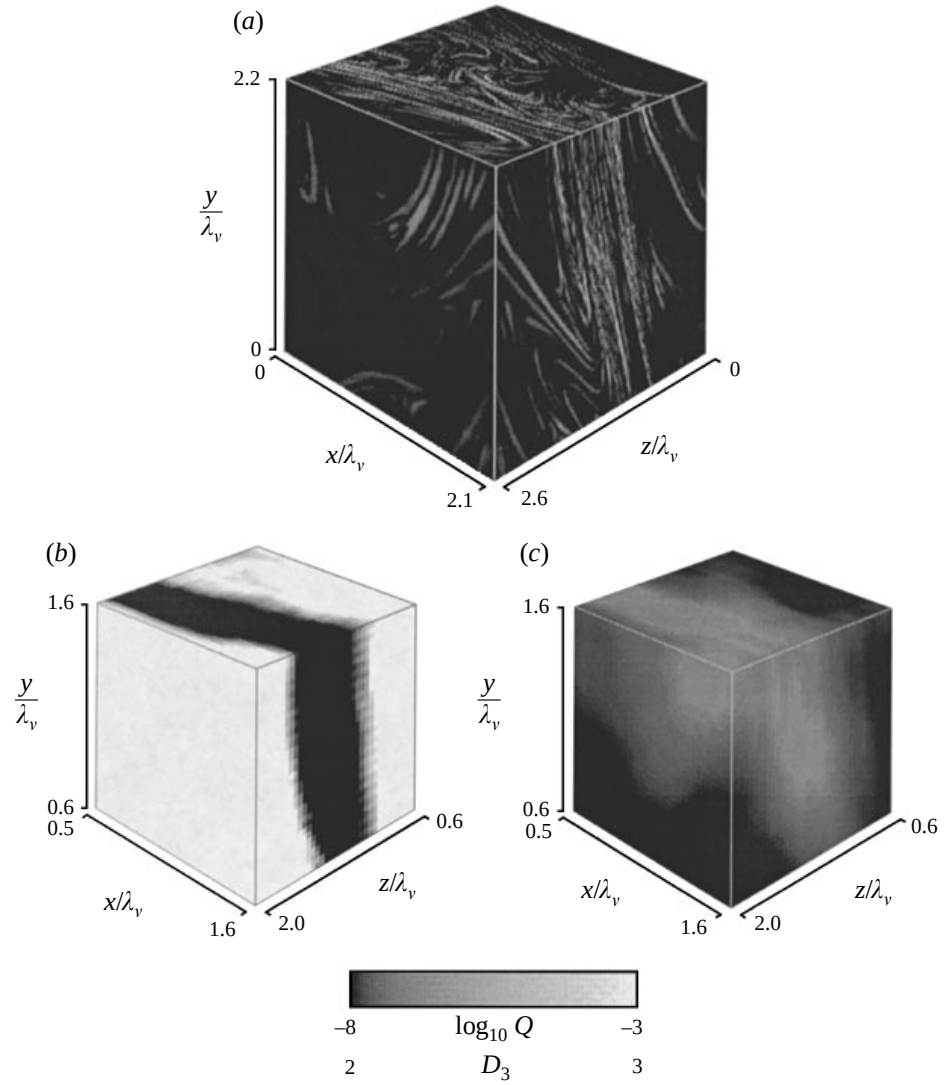

FIGURE 22. (*a*) Local (64^3) scale-similarity results for the dissipation support in the three-dimensional data volume R0703044, which was found to be non-fractal in §5.2. Large regions of significantly non-fractal Q values can be seen in (*b*), which correspond to regions of highly parallel dissipation layers.

the classical Sauter mean diameter, defined from the radius of a sphere having the same volume to surface area ratio as the inclusions. For a single spherical inclusion, this ratio is

$$\frac{\text{Volume}}{\text{Surface area}} \equiv \frac{\frac{4}{3}\pi r^3}{4\pi r^2} = \tfrac{1}{3}r, \tag{3}$$

and thus the Sauter mean radius R_{SMD} for an ensemble of m spherical inclusions effectively gives

$$R_{SMD} = \sum_{i=1}^{m} r_i^3 \Big/ \sum_{i=1}^{m} r_i^2. \tag{4}$$

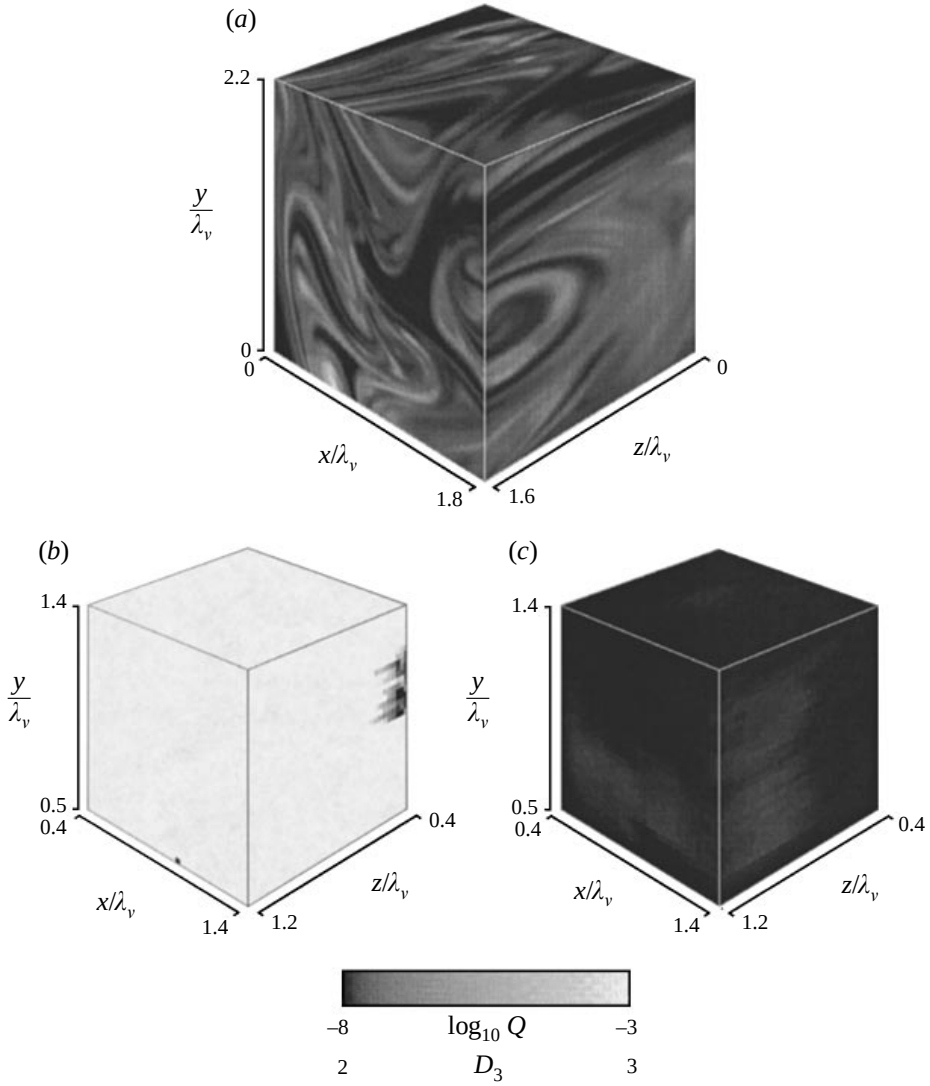

FIGURE 23. (*a*) Local (64^3) scale-similarity results for the dissipation support in the three-dimensional data volume R0304037, which was found to be non-fractal in §5.2. While the Q values in (*b*) appear to suggest scale similarity, the D values in (*c*) lie in a narrow range near $D = 2$, indicating that the scalar isosurfaces over this range of scales are non-fractal and instead correspond to topologically simple surfaces.

However, since most inclusions like those in figures 20–22 lie only partly inside the measurement volume, neither their full volume nor surface area can be directly evaluated. For this reason, a closely related lengthscale is instead defined from a differential surface area ratio as the radius of a sphere having the same rate of change of surface area with radius as the inclusions. This can be readily evaluated so long as any significant part of the inclusion intersects the measurement volume. For a single spherical inclusion, this ratio is

$$\lim_{\epsilon \to 0} \frac{\text{Surface area}\,(r+\epsilon)}{\text{Surface area}\,(r)} \equiv \frac{4\pi(r+\epsilon)^2}{4\pi r^2} \to 1 + \frac{2\epsilon}{r}, \tag{5}$$

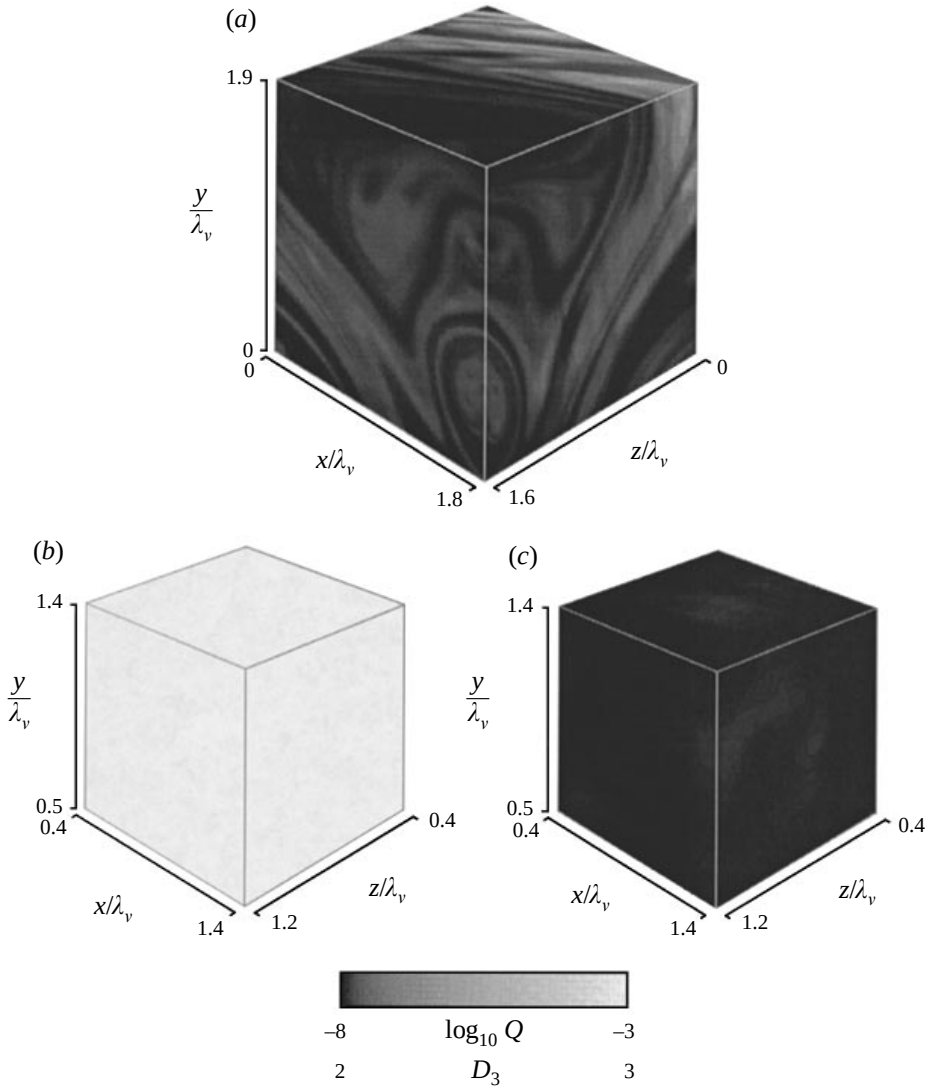

FIGURE 24. (*a*) Local (64^3) scale-similarity results for the dissipation support in the three-dimensional data volume R0304039, which was found to be non-fractal in §5.2. Again the Q values in (*b*) appear to suggest scale similarity, but the D values in (*c*) lie in a narrow range near $D = 2$, indicating that scalar isosurfaces over this range of scales are non-fractal and instead correspond to topologically simple surfaces.

and thus the equivalent radius R_S of an ensemble of m spherical inclusions effectively gives

$$R_S = \sum_{i=1}^{m} r_i^2 \Big/ \sum_{i=1}^{m} r_i, \tag{6}$$

which may be compared with (4). This definition for R_S is equivalent to a concept called the 'surface diameter' D_{12}, typically encountered in adsorption problems, which comes from the same family of diameters in which the Sauter mean diameter is D_{23} as is apparent from (4) and (6).

Here R_S is determined from $Q(\boldsymbol{x}, t)$ fields of the type in parts (*b*) of each of figures 17–22 via (5) from the surface area ratio of two closely spaced iso-Q surfaces near the threshold value $\log_{10} Q \approx -3$ separating locally fractal and non-fractal scalings in figure 15. Results obtained for each individual volume vary rather widely from volume to volume, and even among the three cases. Average values obtained for the three cases give the inclusion radius $R_S/\lambda_\nu \approx 0.62$, 0.23 and 0.65, giving a mean characteristic diameter $2R_S$ of roughly one-half to one-and-a-half viscous diffusion scales λ_ν. This is somewhat larger than the crude estimate in §6.1. However, neither the cubic inclusion model on which those esimates were based nor the spherical model used here are very good representations of the inclusion topology, as can be seen in figures 20–22.

These estimates of the characteristic inclusion lengthscale being of the order of the viscous diffusion scale λ_ν appear consistent with the timescale on which variations in Q are evident in table 3. Indeed the timescale on which Q varies appears comparable to the viscous diffusion scale advection time λ_ν/u. These variations are thus presumably due to inclusions advecting through the measurement volume. Collectively, these results for the scalar dissipation support appear to show that much of the variation with both intersection dimension n and with time in the fraction of intersections found to be fractal are due to the presence of non-fractal inclusions. Although the shape of these inclusions varies widely, their characteristic size is of the order of the viscous diffusion scale λ_ν. Since these non-fractal inclusions generally coincide with regions where many neighbouring scalar dissipation layers have been brought into a nearly parallel sheet-like arrangement by the underlying strain field (e.g. figures 20–22), and since their characteristic lengthscale is of the order of the viscous diffusion scale λ_ν, it appears that they may be spatial manifestations of the expected diffusive cutoff process.

6.5. *Scalar isosurface intersections*

Given the success in reconciling the results obtained for the scale similarity properties of the scalar dissipation support of §§4 and 5 and in Part 1 on the basis of the non-fractal inclusions in §§6.1, 6.3 and 6.4, it is natural to inquire if these inclusions can also account for the somewhat different results found for the geometry of scalar isosurfaces. Accordingly, figures 23 and 24 show typical results obtained when the local scale-similarity analyses of §6.2 are applied to scalar isosurfaces. These figures are analogous to figures 17–22 for the scalar dissipation support geometry, however, it is apparent that the conclusions that must be drawn from them are fundamentally different.

The $Q(\boldsymbol{x}, t)$ fields in part (*b*) of figures 23 and 24 show strong scale similarity throughout the entire volume over the range of lengthscales covered in these smaller 64^3 subvolumes. However, the local dimension values $D_3(\boldsymbol{x}, t)$ in part (*c*) of these figures show that the dimension associated with this smaller range of lengthscales in the scalar isosurfaces is simply $D_3 \equiv 2$, indicating non-fractal structure corresponding to locally sheet-like geometries. This is quite different from the corresponding results for the dissipation support in figures 17–22, which showed fractal scale similarity even at these lengthscales. Note that the volume presented in figure 23 is the same as that in figure 17, yet the dissipation support field shows clearly uniform fractal scaling, whereas the corresponding scalar isosurfaces show only the trivial cutoff to $D = 2$ at these scales. When these results are viewed together with those obtained at larger scales in §§4 and 5 and in Part 1, it must be concluded that strict fractal scale similarity is inapplicable to scalar isosurface geometries over both the inner range of scales, between (λ_D, T_D) and (λ_ν, T_ν), and the outer range of scales, between (λ_ν, T_ν) and (δ, T_δ).

7. Discussion and conclusions

This study has extended the objective statistical techniques developed for scale similarity analyses in Part 1 and has applied them to examine the applicability of uniform fractal scale similarity in two-dimensional (256^2) and three-dimensional (256^3) intersections with fully resolved experimental data for the geometry of scalar isosurfaces and the dissipation support in a turbulent flow. The present study spans the inner range of scales from the scalar diffusion lengthscale λ_D to the viscous diffusion scale λ_ν.

For the spatial support geometry on which the scalar dissipation field $\nabla\zeta \cdot \nabla\zeta(\boldsymbol{x}, t)$ is concentrated over this inner range of scales, Part 1 found 78 % of one-dimensional intersections to be as fractal as 90 % of one-dimensional fBm sets with the same record length. The present study finds that typically 64 % of two-dimensional intersections and 50 % of three-dimensional intersections display uniform scale similarity as fractal as 90 % of stochastically self-similar fBm sets having the same dimension and record length (see tables 3 and 5). None of these intersections showed scaling as random as a corresponding random set. This decrease with increasing intersection dimension n in the percentage of intersections found to be fractal is consistent with the presence of non-fractal inclusions in an otherwise fractal background structure, as discussed in §6.1. Indeed, §6.3 used local scale similarity analyses based on three-dimensional (64^3) spatial intersections to show directly the presence of such non-fractal inclusions in the $Q(\boldsymbol{x}, t)$ fields (see figures 17*b*–22*b*). Intersections passing through these inclusions have their scale similarity interrupted and thus do not meet the objective criteria for fractal scaling. With increasing intersection dimension n, an increasing percentage of intersections contains a significant part of one or more of these inclusions. The shapes of these inclusions vary widely, but their characteristic scale is of the order of λ_ν, as is evident in figures 20–22, and consistent with the measured percentages in table 5. Moreover, the inclusions often coincide in the dissipation fields with regions where the dissipation layers have been brought into a largely parallel arrangement of sheets by the underlying flow field (see figures 17*a*–22*a*), suggesting that they are spatial manifestations of the expected scaling cutoff near the diffusive scale λ_ν.

Consistent with this, the relation $D_n = D-(3-n)$ among codimensions holds only for those intersections that are essentially free of such inclusions. It is only as $Q \to 1$ that $\langle D_2 \rangle$ in figures 6 and 7 approaches the value consistent with this relation from the result $\langle D_1 \rangle \approx 0.66$ obtained in Part 1. When applied to simple average dimensions over both fractal and non-fractal intersections, the relation among codimensions fails.

Similar analyses of the spatial geometry of scalar isosurfaces in the conserved scalar field $\zeta(\boldsymbol{x}, t)$ over the same range of scales show rather different results. Whereas typically 56 % of two-dimensional intersections with the mean scalar isosurface showed scale similarity consistent with 90 % of fBm gauge sets having the same dimension and record length (see figures 8 and 9 and table 3), none of the corresponding three-dimensional intersections were consistent with uniform fractal scale similarity (see figures 13 and 14 and table 3). This reduction with increasing intersection dimension cannot be explained by the presence of non-fractal inclusions found in the dissipation support fields. Instead, the same local scale-similarity analyses demonstrated that the entire scalar isosurface geometry over this range of scales shows only the trivial geometric cutoff to $D_3 \equiv 2$. Consistent with this, the relation among codimensions fails entirely for the scalar isosurface results, as can be seen from table 3.

When the present results are combined with those obtained in Part 1, it must be concluded that the geometry of scalar isosurfaces does not appear consistent with the

concept of uniform fractal scale similarity over any range of scales. In contrast, the geometry of the dissipation support from precisely the same data clearly shows uniform fractal scale similarity, even by the present strictly objective criteria. The apparent fundamentally different scale-similarity properties of the conserved scalar field $\zeta(\boldsymbol{x}, t)$ and the scalar dissipation rate field $\boldsymbol{\nabla}\zeta \cdot \boldsymbol{\nabla}\zeta(\boldsymbol{x}, t)$ may result in part from the differing abilities of these two fields to retain information. Since the scalar isosurface geometry depends on the entire evolution of the conserved scalar field since its initial conditions there is, in this sense, no loss of memory in the scalar field. However, in the scalar dissipation field, as scalar gradient layers merge, their dissipation decreases until it eventually drops below the threshold value and they disappear from the support set. This is evident from the diffusional cancellation term in the dissipation transport equation (e.g. Southerland *et al.* 1991). The information carried by these layers concerning past history of the underlying mixing dynamics is thus lost in the scalar dissipation field. In contrast, the scalar isosurface geometries reflect all the past history, including possible variations in dimension that might preclude applicability of any simple uniform fractal scale-similarity with a single dimension.

As in Part 1 the present finding of fractal scale similarity in the scalar dissipation support appears consistent with the result of Prasad *et al.* (1988). However, the lack of fractal scale similarity in the isoscalar surfaces geometry disagrees with the findings of Sreenivasan & Meneveau (1986), Prasad & Sreenivasan (1990*a*, *b*), Sreenivasan *et al.* (1989) and Sreenivasan (1991). Several possible reasons for this were discussed in Part 1. Those that are relevant to the present study include the fact that the results are based on strict tests for uniform fractal scale similarity over the entire range of scales examined, and the possible effects of the scaling break anticipated across the viscous diffusion scale λ_ν. However, the present results convincingly show uniform fractal scale similarity in the dissipation support field over the same range of scales, and when viewed together with the results from Part 1 show no apparent change in dimension across λ_ν. A second possible reason for the different finding in this study is the potential influence of the inner cutoff scale. Clear evidence of this inner cutoff was found in the scalar isosurface fields in §6.5, however, this in no way interfered with the ability to assess the scale similarity over this range of scales. Moreover, on the same range of scales, the dissipation support geometry in the present study clearly showed fractal scale-similarity, and further was even able to convincingly identify with the manifestations of this inner cutoff process via the localized inclusions found in §6.3 and figures 17–22. It is also possible that the present Re_λ values may not be sufficiently large. However, these Reynolds numbers are not very different from other studies, and, more importantly, the clear evidence for uniform fractal scale similarity in the dissipation support fields from precisely the same data suggests that this is not likely to be the case. It is concluded that the different results concerning the applicability of fractal scale similarity to scalar isosurfaces are due to the strictly objective statistical criterion used here for judging data records to be as fractal as known fractal gauge sets having the same dimension and record lengths.

The scalar dissipation support geometry in turbulent shear flows, over the range of record lengths and the range of lengthscales and timescales accessible in this study and in Part 1, thus appears to be representable by stochastic fractal scale similarity of the type embodied in fBm sets. However, the scalar isosurface geometry over the same range of scales does not appear to follow fractal scale similarity.

The three- and four-dimensional scalar field data used in this study were obtained at Michigan as part of the doctoral dissertation work of Dr Kenneth B. Southerland,

under support from the Air Force Office of Scientific Research (AFOSR) Airbreathing Combustion program under Grant No. AFOSR-89-0541 and the Turbulence Structure and Control program under Grant No. F49620-92-J-0025.

REFERENCES

BEVINGTON, P. R. & ROBINSON, D. K. 1992 *Data Reduction and Error Analysis for the Physical Sciences*. McGraw-Hill.

DAHM, W. J. A., SOUTHERLAND, K. B. & BUCH, K. A. 1991 Direct, high-resolution, four-dimensional measurements of the fine scale structure of $Sc \gg 1$ molecular mixing in turbulent flows. *Phys. Fluids* A **3**, 1115–1127.

EVERSON, R. M. & SREENIVASAN, K. R. 1992 Accumulation rates of spiral-like structures in fluid flows. *Proc. R. Soc. Lond.* A **437**, 391–401.

FEDER, J. 1988 *Fractals*. Plenum Press.

FREDERIKSEN, R. D., DAHM, W. J. A. & DOWLING, D. R. 1996 Experimental assessment of fractal scale similarity in turbulent flows. Part 1. One-dimensional intersections. *J. Fluid. Mech.* **327**, 35–72.

FREDERIKSEN, R. D., DAHM, W. J. A. & DOWLING, D. R. 1997 Experimental assessment of fractal scale similarity in turbulent flows. Part 3. Multifractal scaling. *J. Fluid. Mech.* **338**, 127–155.

JIMÉNEZ, J., WRAY, A. A., SAFFMAN, P. G. & ROGALLO, R. S. 1993 The structure of intense vorticity in isotropic turbulence. *J. Fluid Mech.* **255**, 65–90.

KOLMOGOROV, A. N. 1941 Local structure of turbulence in an incompressible fluid at very high Reynolds numbers. *C.R. Acad. Sci. URSS* **30**, 301–305.

KOLMOGOROV, A. N. 1962 A refinement of previous hypotheses concerning local structure of turbulence in viscous incompressible fluid at high Reynolds number. *J. Fluid Mech.* **13**, 82–85.

KUSCH, H. A. & OTTINO, J. M. 1992 Experiments on mixing in continuous chaotic flows. *J. Fluid Mech.* **236**, 319–348.

LANE-SERFF, G. F. 1993 Investigation of the fractal structure of jets and plumes. *J. Fluid Mech.* **249**, 521–534.

OTTINO, J. M., MUZZIO, F. J., TJAHJADI, N., FRANJIONE, J. G., JANA, S. C. & KUSCH, H. A. 1992 Chaos, symmetry and self-similarity: exploiting order and disorder in mixing processes. *Science* **257**, 754–760.

PRASAD, R. R., MENEVEAU, C. & SREENIVASAN, K. R. 1988 The multifractal nature of the dissipation field of passive scalars in fully turbulent flows. *Phys. Rev. Lett.* **61**, 74–77.

PRASAD, R. R. & SREENIVASAN, K. R. 1990*a* The measurement and interpretation of fractal dimensions of the scalar interface in turbulent flows. *Phys. Fluids* A **2**, 792–807.

PRASAD, R. R. & SREENIVASAN, K. R. 1990*b* Quantitative three-dimensional imaging and the structure of passive scalar fields in fully turbulent flows. *J. Fluid Mech.* **216**, 1–34.

PRESS, W. H., TEUKOLSKY, S. A., VETTERLING, W. T. & FLANNERY, B. P. 1992 *Numerical Recipes in FORTRAN: The Art of Scientific Computing*. Cambridge University Press.

SOUTHERLAND, K. B. & DAHM, W. J. A. 1994 A four-dimensional experimental study of conserved scalar mixing in turbulent flows. *Report No. 026779-12*, Department of Aerospace Engineering, The University of Michigan, Ann Arbor, MI.

SOUTHERLAND, K. B. & DAHM, W. J. A. 1996 Fully resolved four-dimensional measurements of the small-scale structure of passive scalar mixing in turbulent flows. Submitted to *J. Fluid Mech.*

SOUTHERLAND, K. B., DAHM, W. J. A. & DOWLING, D. R. 1995 Experimental results for the high wavenumber spectral structure of scalar mixing in turbulent shear flows. In *Proc. 10th Symp. Turb. Shear Flows*, Pennsylvania State University, University Park, PA.

SOUTHERLAND, K. B., PORTER, J. R., DAHM, W. J. A. & BUCH, K. A. 1991 An experimental study of the molecular mixing process in an axisymmetric laminar vortex ring. *Phys. Fluids* A **3**, 1385–1392.

SREENIVASAN, K. R. 1991 Fractals and multifractals in fluid turbulence. *Ann. Rev. Fluid Mech.* **23**, 539–600.

Sreenivasan, K. R. & Juneja, A. 1993 Fractal dimensions of time series in turbulent flows. (Unpublished manuscript.)

Sreenivasan, K. R. & Meneveau, C. 1986 The fractal facets of turbulence. *J. Fluid Mech.* **173**, 357–386.

Sreenivasan, K. R. & Prasad, R. R. 1989 New results on the fractal and multifractal structure of the large Schmidt number passive scalars in fully turbulent flows. *Physica* D **38**, 322–329.

Sreenivasan, K. R., Ramshankar, R. & Meneveau, C. 1989 Mixing, entrainment, and fractal dimensions of surfaces in turbulent flows. *Proc. R. Soc. Lond.* A **421**, 79–108.

Vassilicos, J. C. & Hunt, J. C. R. 1991 Fractal dimensions and spectra of interfaces with application to turbulence. *Proc. R. Soc. Lond.* A **435**, 505–534.